Rotational alignment effects in NO(X) + Ar inelastic collisions: A theoretical study

M. Brouard,[1, a)] H. Chadwick,[1] C.J. Eyles,[1, b)] B. Hornung,[1] B. Nichols,[1] F.J. Aoiz,[2, c)] P.G. Jambrina,[2] S. Stolte,[3] and M.P. de Miranda[4]

[1)] *The Department of Chemistry, University of Oxford, The Physical and Theoretical Chemistry Laboratory, South Parks Road, Oxford, OX1 3QZ, United Kingdom.*

[2)] *Departamento de Química Física, Facultad de Química, Universidad Complutense, 28040 Madrid, Spain*

[3)] *Atomic and Molecular Physics Institute, Jilin University, Changchun 130012, China*[d)]

[4)] *School of Chemistry, University of Leeds, Leeds, LS2 9JT, United Kingdom*

(Dated: 3 January 2013)

Rotational angular momentum alignment effects in the rotational inelastic scattering of NO(X) with Ar have been investigated by means of close-coupled quantum mechanical, quasi-classical trajectory, and Monte Carlo hard shell scattering calculations. It has been shown that the hard shell nature of the interaction potential at a collision energy of $E_{\rm coll} = 66\,$meV is primarily responsible for the rotational alignment of the NO(X) molecule after collision. By contrast, the alternating trend in the quantum mechanical parity resolved alignment parameters with change in rotational state Δj reflects differences in the differential cross sections for NO(X) parity conserving and changing collisions, rather than an underlying difference in the collision induced rotational alignment. This suggests that the rotational alignment and the DCSs are sensitive to rather different aspects of the scattering dynamics. The applicability of the kinematic apse model has also been tested and found to be in excellent agreement with exact quantum mechanical scattering theory providing the collision energy is in reasonable excess of the well depth of the NO(X)–Ar potential energy surface.

[a)] Electronic mail: mark.brouard@chem.ox.ac.uk

[b)] Current address: Institut fur Chemie und Biochemie, Freie Universitat Berlin, Takustr. 3 14195 Berlin, Germany.

[c)] Electronic mail: aoiz@quim.ucm.es

[d)] Alternative affiliations: Laser Center, Vrije Universiteit, Amsterdam, De Boelelaan 1083, 1081 HV Am-

sterdam, The Netherlands and Laboratoire Francis Perrin, Bâtiment 522, DRECEM/SPAM/CEA Saclay, 91191 Gif sur Yvette, France

I. INTRODUCTION

Investigating vector correlations in atomic and molecular collisions reveals valuable information on the underlying dynamics, particularly on the forces governing such interactions.[1,2] The pair correlation between the initial and final relative velocity, $\boldsymbol{k}$ and $\boldsymbol{k}'$, and the triple correlation between the initial and final relative velocity and the final rotational angular momentum, $\boldsymbol{j}'$, are of particular interest.[3,4] The former is characterized by the conventional differential cross section (DCS), or the angular distribution of the scattered products, while the latter manifests itself as scattering angle dependent rotational angular momentum polarization.

Collisions of ground state NO(X) with the noble gases have served as a prototype for the study of the interactions between open shell diatomic molecules and closed shell atoms.[5,6] The electronic ground state of NO(X) has an electron configuration $1\sigma^2 1\sigma^{*2} 2\sigma^2 2\sigma^{*2} 1\pi^4 3\sigma^2 1\pi^{*1}$, and in low rotational states the resulting NO($X^2\Pi$) ground state can be characterized approximately according to a Hund's case (a) coupling scheme. This gives rise to wavefunctions labeled by the quantum numbers $|\Omega, j, \epsilon\rangle$, where j is the rotational quantum number, and Ω is the absolute value of the electronic angular momentum along the internuclear axis. The ground state of NO(X) is therefore split into two spin-orbit manifolds, $\Omega = 1/2$ and $\Omega = 3/2$, with a splitting constant of $123\,\mathrm{cm}^{-1}$. For higher rotational states an intermediate case (a)/case (b) coupling scheme has to be employed. Because of the interaction between the electronic orbital and rotational angular momenta, the degeneracy of each rotational level is lifted, yielding two Λ-doublet components which differ in their parity. The latter is determined by considering the space-fixed inversion operator E^*, $E^*\psi = \pm\psi$. If an NO(X) molecule in a specific quantum state is symmetric with respect to inversion, the state has a positive parity, $p = +1$, while if it is antisymmetric it has a negative parity, $p = -1$. This parity is related to the symmetry or spectroscopic parity index, ϵ, by $\epsilon = p(-1)^{j-1/2}$, or equivalently $p = \epsilon(-1)^{j-1/2}$. Λ-doublet components with $\epsilon = +1$ are designated by the label e, the $\epsilon = -1$ levels by the label f. The f levels are slightly higher in energy than the e. In addition to the labels e and f, the NO(X) Λ-doublet levels are often labeled as A' or A'', depending on whether the electronic wave function is symmetric or antisymmetric with respect to reflection in the plane of rotation of the NO(X) molecule. In the high j limit, the unpaired electron lies in the plane of rotation in the A' states, and lies perpendicular to

that plane in the A″ states.[7]

On approach of an Ar atom to the NO(X) molecule in non-linear configurations, the $^2\Pi$ state splits into ^{2}A′ and ^{2}A″ electronic states. Alexander[5,6] has shown that in the Hund's case (a) limit, spin-orbit conserving transitions are coupled by a $V_{\rm sum}$ potential, defined as

$$V_{\rm sum}(\gamma, R) = \frac{1}{2}\left[V_{\rm A'}(\gamma, R) + V_{\rm A''}(\gamma, R)\right] = \sum_{l=0}^{\infty} V_{l0}(R) d^l_{00}(\gamma)\,, \tag{1}$$

while spin-orbit changing collisions are coupled by a difference potential,

$$V_{\rm diff}(\gamma, R) = \frac{1}{2}\left[V_{\rm A'}(\gamma, R) - V_{\rm A''}(\gamma, R)\right] = \sum_{l=2}^{\infty} V_{l2}(R) d^l_{20}(\gamma)\,. \tag{2}$$

In these equations, $V_{\rm A'}$ and $V_{\rm A''}$ are the two lowest lying states of the CCDS(T) potential energy surfaces (PESs) for the Ar–NO(X) system. R is the distance between the argon atom and the centre-of-mass of the diatom, and γ is the angle between $\boldsymbol{R}$ and the NO bond axis, $\boldsymbol{r}$, which points from O to N. $V_{l\lambda}(R)$ are radial-dependent expansion coefficients, and $d^l_{q0}(\gamma)$ is a Wigner reduced rotation d-matrix element.

The NO(X) + Ar system has been of much theoretical and experimental interest. Accurate potential energy surfaces have been constructed[8,9] on which extensive scattering calculations have been performed. The primary focus of many of these studies has been on the integral[8] and differential[10–13] cross sections, particularly more recently on explaining parity dependent structure in the integral[8] and differential[11–13] cross sections. The integral cross sections show periodic alternations in magnitude as a function of j' and of the NO(X) parity changing/conserving nature of the transition. In addition, the form of the DCSs, in particular the number of maxima and minima as a function of scattering angle, depends on the change in the total parity of the NO(X) molecule on collision.[11–13] Λ-doublet resolved DCSs have been measured recently using velocity map ion-imaging, and have been shown to be in excellent agreement with QM scattering theory.[11–13]

Relatively fewer investigations have been directed towards polarization effects in this collision system. The collision-induced alignment of NO(X), averaged over the unselected initial Λ-doublet level, was first measured experimentally by Cline *et al.*[14] and Wade *et al.*[15] For the low j' states they found reasonable agreement between the experiment and the close-coupled quantum mechanical (CC QM) scattering theory results obtained using the CCSD(T) PESs of Alexander.[8] They also showed that the CC QM alignment data were

in excellent agreement with the predictions of a simple rigid ellipse model, though both calculations showed somewhat more alignment than observed experimentally.[14,15]

Early theoretical work by Alexander established propensity rules for the QM cross sections involving magnetic level, m_j, resolved transitions for NO(X) + Ar.[16] Rotational polarization effects have also been investigated using quasi-classical trajectory (QCT) methods by Aoiz *et al.*[17] These calculations were performed on the $V_{\rm sum}$ PES, and their results reproduced well the quantum mechanical ones, once the latter were averaged over the initial, and summed over the final Λ-doublet states. The authors also looked at the role of chattering collisions in rotationally inelastic scattering in this system.[17] They provided a definition of chattering encounters, and showed that, while chattering collisions do play some role in NO(X) + Ar in cooling the final rotational excitation compared with non-chattering collisions, they tend to result in lower angular momentum polarization than non-chattering collisions.[17] In a recent theoretical study of NO(X) scattering by the rare gases, Lemeshko *et al.* have described the alignment effects in the forward scattered region in terms of a Fraunhofer diffraction model.[18] This model accurately describes the oscillatory rotational alignment in the extreme forward scattered region, where diffraction effects dominate, but says little about the rotational polarization in the sideways and backward directions. Finally, most recently, Jambrina *et al.* have studied the collision induced angular momentum orientation of the NO(X) after scattering by Ar using canonical collision mechanisms theory.[19]

As will be seen from the present work, the linear momentum transfer vector is of considerable importance in non-reactive impulsive collisions.[20,21] It is helpful to introduce the *kinematic apse*, $\hat{\boldsymbol{a}}$, defined as the unit vector pointing in the direction of the linear momentum transfer,

$$\hat{\boldsymbol{a}} = \frac{(\boldsymbol{p}' - \boldsymbol{p})}{|\boldsymbol{p}' - \boldsymbol{p}|}\,, \tag{3}$$

where $\boldsymbol{p}$ and $\boldsymbol{p}'$ are the initial and final linear momenta. For elastic and inelastic scattering, the kinematic apse can also be written in terms of the relative velocities, $\hat{\boldsymbol{a}} = (\boldsymbol{k}' - \boldsymbol{k})/(|\boldsymbol{k}' - \boldsymbol{k}|)$. In the case of sudden collisions between impenetrable objects, the projection of $\boldsymbol{j}'$ onto the kinematic apse remains unchanged; this behavior is the basis of the kinematic apse model.[20,21] It can be rigorously proven classically for rigid objects.[20,21] It is worth mentioning in passing that an alternative model, the geometric apse model, is derived from the kinematic apse model, but assumes elastic collisions.[22] The applicability of the kinematic apse model has not been tested quantum mechanically, although it has been used to correct experimental

ion-images for collision-induced rotational alignment effects.[11,12,23] Furthermore, as noted above, the CC QM and rigid ellipse alignment data were shown by Wade *et al.* to be in excellent agreement with each other.[15] However, the fact that the calculated alignment was found to be larger in magnitude than the experimental data was taken to imply that more work was needed to improve the repulsive part of the NO(X)–Ar PES.[15] Experimental studies by H. Meyer have shown that the collision induced alignment in NO(X) + He and Ne collisions conforms well to the kinematic apse model.[22]

The aim of the present paper is to report a comparative investigation into the origin of the rotational alignment effects in the rotationally inelastic collisions of NO(X) and Ar. We consider the alignment effects in the $|\Omega = \frac{1}{2}, j = 0.5, e/f\rangle \longrightarrow |\Omega' = \frac{1}{2}/\frac{3}{2}, j', e/f\rangle$ collisions of electronically and vibrationally ground state NO. The effect of the DCSs on the averaged alignment properties was also examined. Classical homonuclear and heteronuclear hard shell Monte Carlo, QCT, and CC QM calculations were employed. The paper is organized as follows. In section II, the theoretical methods used to obtain differential cross sections and polarization information on the collision system are described. In section III the results are presented and discussed, and the main findings of the paper are summarized in section IV.

In the accompanying paper,[24] the conclusions of the present theoretical study will be confirmed through experimental measurement of the collision-induced angular momentum alignment at the fully quantum state resolved level.

II. THEORY AND METHODS

A. Polarization dependent differential cross sections and polarization parameters

The principal frame used throughout this paper is the scattering (or collision) frame, in which the z-axis lies parallel to the initial relative velocity of the collision partners, $\boldsymbol{k}$. The final relative velocity of the colliding partners after the collision, $\boldsymbol{k}'$, is taken to lie in the $x > 0$ half of the xz-plane, while the y-axis is chosen to have a right handed frame of reference. The scattering angle, θ, is defined as the angle between $\boldsymbol{k}$ and $\boldsymbol{k}'$.

The classical probability of a particle being scattered into a solid angle θ with its angular

momentum pointing towards $(\theta_{j'}, \phi_{j'})$ is denoted $P(\cos\theta, \cos\theta_{j'}, \phi_{j'})$. This probability can be expressed in terms of a series expansion in the modified spherical harmonics, $C^*_{kq}(\theta_{j'}, \phi_{j'})$,[25]

$$P(\cos\theta, \cos\theta_{j'}, \phi_{j'}) = \sum_{kq} \frac{2k+1}{4\pi} \left(\frac{2\pi}{\sigma} \frac{\mathrm{d}\sigma_{kq}}{\mathrm{d}\omega} \right) C^*_{kq}(\theta_{j'}, \phi_{j'}) \,, \tag{4}$$

where the expansion coefficients $(2\pi/\sigma)\mathrm{d}\sigma_{kq}/\mathrm{d}\omega$ are the normalized polarization dependent differential cross sections (PDDCSs).[25,26] These expansion coefficients characterize the spatial polarization of the angular momentum of the scattered particles as a function of the scattering angle. The $k = 0$, $q = 0$ normalized PDDCS quantifies the angular distribution of $\boldsymbol{k}'$ about $\boldsymbol{k}$, and is proportional to the differential cross section, *i.e.* $\mathrm{d}\sigma_{00}/\mathrm{d}\omega = \mathrm{d}\sigma/\mathrm{d}\omega$.

The polarization parameters, $a^{(k)}_q$, are defined according to the equation

$$a^{(k)}_q = \frac{2\pi}{\sigma} \int_{-1}^{+1} \frac{\mathrm{d}\sigma_{kq}}{\mathrm{d}\omega} \, \mathrm{d}\cos\theta \,. \tag{5}$$

They quantify the total multipolar contribution of rank k and component q to the distribution function integrated over all scattering angles.

It is possible to introduce a conditional probability distribution of $\boldsymbol{j}'$ being polarized with angles $(\theta_{j'}, \phi_{j'})$ at a given scattering angle, θ:

$$\begin{aligned} P(\cos\theta_{j'}, \phi_{j'} | \cos\theta) &= \sum_{kq} \frac{2k+1}{4\pi} \left(\frac{\mathrm{d}\sigma_{kq}}{\mathrm{d}\omega} \Big/ \frac{\mathrm{d}\sigma}{\mathrm{d}\omega} \right) C^*_{kq}(\theta_{j'}, \phi_{j'}) \\ &= \sum_{kq} \frac{2k+1}{4\pi} \rho^{(k)}_q(\theta) \, C^*_{kq}(\theta_{j'}, \phi_{j'}) \,. \end{aligned} \tag{6}$$

Here, the expansion coefficients, $\rho^{(k)}_q(\theta)$, are referred to as the *renormalized* PDDCSs,[3,25] defined by the term in brackets in the first of the above equations.

Quantum mechanically, the renormalized PDDCSs appear as the expansion coefficients of the scattering density matrix. The scattering angle resolved density matrix of the final state is given by the equation

$$\langle j'm'_1 | \rho(\cos\theta) | j'm'_2 \rangle = \sum_{kq} \frac{(2k+1)}{2j'+1} \, \rho^{(k)}_q(\theta) \, \langle j'm'_1, kq | j'm'_2 \rangle \,, \tag{7}$$

where $\langle j_1 m_1, j_2 m_2 | j_3 m_3 \rangle$ is a Clebsch-Gordon coefficient.[27] The diagonal elements of the density matrix, $\langle j'm' | \rho(\cos\theta) | j'm' \rangle$, represent the population in the different magnetic quantum levels, whilst the off-diagonal elements reveal information about the coherences existing between different eigenstates, which are essential for the azimuthal polarization of $\boldsymbol{j}'$. In

general, the PDDCSs and polarization parameters are complex. However, it is possible to introduce real quantities as a linear combination of the complex moments. The advantage of the real polarization moments is that they have immediate directional meanings that complex moments lack, and are also QM observables associated with Hermitean operators. Using the Hertel-Stoll definition[28] of real polarization moments, denoted by $a_{q\pm}^{\{k\}}$ or $\rho_{q\pm}^{\{k\}}$, these moments can be written

$$\begin{aligned} a_0^{\{k\}} &= a_0^{(k)} && \text{for} \quad q = 0 \\ a_{q+}^{\{k\}} &= \frac{1}{\sqrt{2}} \left[(-1)^q a_q^{(k)} + a_{-q}^{(k)} \right] && \text{for} \quad q > 0 \\ a_{q-}^{\{k\}} &= \frac{1}{\sqrt{2}i} \left[(-1)^q a_q^{(k)} - a_{-q}^{(k)} \right] && \text{for} \quad q > 0\,. \end{aligned} \tag{8}$$

Real PDDCSs and real renormalized PDDCSs are defined in an analogous way.

B. Quantum mechanical close-coupled calculations

Full non-adiabatic close-coupled calculations were carried out using the HIBRIDON[29–31] program suite on the $V_{\rm sum}$ and $V_{\rm diff}$ CCSD(T) PESs of Alexander.[8] The PESs were obtained for a fixed equilibrium bond length of the NO(X) molecule, and so the scattering calculations do not take into account the vibrational degree of freedom of the NO(X) molecule. The collision energy used in most of the QM calculations was $E_{\rm coll} = 66\,\text{meV} = 532\,\text{cm}^{-1}$, which is close to that used in several crossed molecular beam experiments.[11,12,15,32,33] For comparison, calculations were also performed at 15 meV and 30 meV. Rotational states up to $j' = 20.5$, and both Λ-doublet levels ($\epsilon = +1, \epsilon = -1$) and spin-orbit manifolds ($\Omega = 1/2, \Omega = 3/2$) were included in the open-shell scattering wave function. The maximum total angular momentum was set to $J = 160.5$ in order to achieve convergence. This corresponds to a classical impact parameter $b = 6.8\,\text{Å}$.

The DCSs and PDDCSs were obtained from the S-matrix after transformation of the S-matrix from the orbital angular momentum to the helicity representation. The representation transformation used the standard formula,[34] and the calculation of vector properties was performed as described in Refs. 25 and 35. To compare with closed shell quasi-classical and hard shell calculations, the DCSs and PDDCSs were averaged over the initial and summed over the final Λ-doublet levels.

C. Quasi-classical trajectory calculations

The details of the quasi-classical trajectory calculations employed in this work are given elsewhere,[10,36] and only those aspects that are specific to this work are described here. The trajectory calculations employed the same $V_{\rm sum}$ PES as used in the QM scattering calculations.[8] As with the QM calculations, this PES was obtained at fixed NO(X) equilibrium bond length ($r_{\rm e}$) and hence during integration of the equations of motion the value of r was kept fixed at $r_{\rm e}$ by using the method of Lagrangian multipliers.[10,37] The square of the classical angular momentum was equated to $j'(j'+1)\hbar^2$, and the values of j' were then rounded to the nearest integer. The maximum value of the impact parameter was determined as 6.3 Å, beyond which no trajectories exist leading to final states of $j' \geq 0.5$.

As in the QM calculations, for the majority of the results presented the collision energy was set to 66 meV, with the NO(X) molecule initially in its lowest rotational state, ($j = 0$). For comparison, as with the QM calculations, further calculations were also performed at 15 meV and 30 meV. Once the scattering angle was determined for each trajectory, the DCSs were calculated using a Legendre moment expansion, and the PDDCSs were obtained by spherical harmonic expansion. A batch of 3.6×10^6 trajectories was processed to gain scattering and polarization information.

D. Hard shell Monte Carlo calculations

The interaction potential between NO(X) and Ar is mainly repulsive; the attractive forces are not expected to play a dominant role at the collision energy of 66 meV. Thus, it might be thought reasonable to model the collisions with a hard shell interaction potential, corresponding to a purely repulsive PES (*i.e.* to a potential which is zero outside a given contour and infinite inside).

The method of Beck and Ross was adopted.[38,39] Two sets of calculations were performed in which the hard shell potential was adapted to model a homonuclear and a heteronuclear NO(X) molecule. In the homonuclear case, the ground state of the NO(X) molecule was represented by an ellipsoid of $D_{\infty h}$ symmetry. The major and minor semi-axes of the ellipsoid were obtained from Alexander's CCSD(T) $V_{\rm sum}$ PES, setting all odd terms in the expansion of the potential equal to zero. The contour of the resultant potential energy surface was

taken at a collision energy of 66 meV. The major and minor semi-axes of the ellipsoid were found to be 3.46 Å and 2.95 Å, respectively. The point of contact, at which the rigid sphere hits the ellipse, and the surface normal were determined analytically.[38,39] A total of 1.0×10^7 inelastic trajectories were analyzed.

In order to obtain differential cross sections and polarization information in the case in which NO(X) was treated as a hard shell heteronuclear molecule, the method described above was slightly modified. The NO(X) molecule was treated as a surface of revolution of $C_{\infty v}$ symmetry. The two dimensional contour was obtained by determining the set of points that corresponds to the contour curve on the $V_{\rm sum}$ potential at 66 meV. This set of points was then fit to an expansion in Legendre polynomials. A one dimensional simplex algorithm[40] was employed to determine the point of contact, and the surface normal was calculated numerically. A batch of 7×10^6 inelastic trajectories was processed in order to obtain differential cross sections and PDDCSs.

III. RESULTS AND DISCUSSION

A. Differential cross sections

1. Comparison of homonuclear and heteronuclear hard shell DCSs

Differential cross sections from the homonuclear (HOHS) and heteronuclear (HEHS) hard shell classical Monte Carlo calculations are compared in Fig. 1 for a range of different final rotational states. In the homonuclear case, the differential cross sections are all single peaked in the forward or sideways scattering region. The maximum in the angular distribution is followed by a fast decay of the scattering intensity towards large scattering angles. The rotational rainbow angle at which the transition becomes classically allowed is determined by the amount of linear momentum which can be transferred into the rotational degree of freedom of the diatom.[41,42] Within the infinite order sudden approximation (IOS),[13,43] in which the rotational level spacing is assumed to be continuous compared with the collision energy, the highest achievable rotational angular momentum excitation from $j = 0$ is given by

$$\Delta j_{\rm max} = 2k(A - B)\,, \tag{9}$$

where $k = p/\hbar$ is the wave vector, and A and B are the major and minor semi-axes of the molecule, respectively. The rainbow angle is determined by the ratio of the final rotational angular momentum j' and $\Delta j_{\max}$, where

$$\theta_{\mathrm{R}} = 2\sin^{-1}(j'/\Delta j_{\max})\,. \tag{10}$$

When $j'/\Delta j_{\max}$ is greater than unity a classical transition cannot take place. The calculated IOS rainbow angles are marked by the vertical black arrows with crosses in the panels of Fig. 1. They are in good agreement with the Monte Carlo hard shell model rainbow angles. For higher j' states, the difference between the corresponding rainbow angles starts to increase, since the basic assumption of the IOS theory, that of closely spaced rotational levels, does not hold for these transitions.

A physically more faithful treatment of the NO(X) molecule is to represent it as a heteronuclear egg-shaped hard shell. The N-end and the O-end of the molecule are then distinguishable, and two sets of minor and major semi-axes can be linked to the molecule. Interestingly, this results in double peaked differential cross sections, at least within this classical model, as is also shown in Fig. 1, similar to those that were reported for the NO(X) + He collisions.[44,45] The IOS rainbow angles are again indicated in the figure.[43] The agreement between the IOS rainbow angles and the end of the classically forbidden region from the heteronuclear Monte Carlo calculation is good until $\Delta j \sim 11$. For higher j' values, the agreement breaks down, for the reasons already discussed.

2. Comparison of QM, QCT, and heteronuclear hard shell DCS

Comparison of the QM, QCT, and HEHS DCSs provides some insight into quantum effects, and the role of attractive forces. As shown in Fig. 2, for low Δj transitions the QCT DCSs are approximately one order of magnitude larger than those from the HEHS calculations, consistent with the dominant role of attractive forces for these inelastic collisions. As Δj increases, the magnitude of the QCT and HEHS DCSs become more similar. For high Δj, the HEHS DCSs are somewhat larger than the QCT ones. As noted in a previous QCT study of NO(X) + Ar,[17] if a great amount of linear momentum is transferred to the rotational degrees of freedom of the molecule, so that the atom slows down, a secondary, so-called chattering, collision can occur by which the degree of rotational excitation can be

reduced.[15,17,33] The result of this cooling is that the population of high rotational states of NO(X) after collision is reduced. Note that the HEHS model does not predict any significant chattering when the correct dimensions of the ellipsoid are employed. Fig. 2 also illustrates that the classically forbidden region is reduced towards smaller scattering angles when attractive forces are included in the interaction potential, reflecting the fact that inelastic scattering can take place at higher impact parameters when attractive interactions are included.

Although the IOS approximation cannot be applied to the full potential, some multiple peak structure can still be observed in the QCT differential cross sections. Nevertheless, the clear double peaked structure seen in the HEHS calculations is almost completely washed-out when the full potential is employed in the QCT calculations.

Fig. 2 also shows the CC QM differential cross sections, averaged over the initial and summed over the final NO(X) Λ-doublet levels. The QCT and averaged CC QM DCSs have been compared in detail previously in the literature,[10,13] and thus will not be discussed here. However, it is worth emphasizing that the agreement between the averaged CC QM and QCT DCS data is reasonable, as seen from Fig. 2.

B. The renormalized PDDCSs and rank 2 alignment parameters

1. The CC QM renormalized PDDCSs

The open shell DCSs and PDDCSs from the CC QM calculations are shown in Fig. 3 for a selection of spin-orbit conserving transitions. Data for the Λ-doublet resolved transitions $f \rightarrow f$ and $f \rightarrow e$ are compared. As reported previously in the literature, the DCSs depend sensitively on whether or not the NO(X) parity is conserved on collision.[11–13,46] The origin of this effect has been discussed in several places in the literature,[9,13,45] and can be considered as a parity dependent interference phenomenon.

The second rank ($k = 2$) renormalized PDDCSs, $\rho_{q\pm}^{\{k\}}(\theta)$, represent the alignment of $\boldsymbol{j}'$ in the scattering frame. For low Δj and small scattering angles all three second rank CC QM PDDCSs show rapid oscillatory structure due to quantum interferences, which can be described well by a Fraunhofer diffraction model.[18] As Δj increases, the amplitude and extent of the oscillations are reduced, and weak parity dependent undulations in the

renormalized PDDCSs can be observed in the fully Λ-doublet resolved PDDCSs. As with the parity resolved DCSs,[11–13] the detailed structure depends on whether the NO(X) parity is conserved or not during collision. However, interestingly Fig. 3 demonstrates that the angular momentum alignment of the scattered NO(X) is relatively insensitive to the change in NO(X) parity on collision compared with the DCSs. This suggests that the rotational alignment and the DCSs are sensitive to rather different aspects of the scattering dynamics.

Fig. 4 presents the CC QM PDDCSs data averaged over the initial and summed over the final Λ-doublet states for spin–orbit conserving transitions. Once averaged over parity states, the oscillations in the CC QM PDDCSs are almost completely washed out, as seen from the data shown in Fig. 4. Note, furthermore, that the general form of the Λ-doublet averaged alignment is very similar to the Λ-doublet resolved data shown in Fig. 3. In the classical high-j limit, the $\rho_0^{\{2\}}(\theta)$ PDDCS ranges from -0.5 to $+1$, corresponding to $\boldsymbol{j}'$ aligned perpendicular and parallel to $\boldsymbol{k}$, respectively. When the scattering angle is 0° or 180°, $\boldsymbol{j}'$ must be aligned perpendicular to the z-axis. The reason for this is that since the initial $|\boldsymbol{j}|$ is almost zero ($j = 1/2$), the total angular momentum, $\boldsymbol{J}$, is perpendicular to $\boldsymbol{k}$, and hence also to $\boldsymbol{k}'$ at 0° and 180°. Because $\boldsymbol{\ell}$ is also perpendicular to $\boldsymbol{k}'$, then irrespective of its magnitude $\boldsymbol{j}'$ must also be perpendicular to both $\boldsymbol{k}$ and $\boldsymbol{k}'$ at these extreme scattering angles. After a sudden increase in $\rho_0^{\{2\}}(\theta)$ as one moves away from $\theta = 0$, $\boldsymbol{j}'$ is generally weakly aligned parallel to $\boldsymbol{k}$ in the forward scattered region, and then $\rho_0^{\{2\}}(\theta)$ monotonically decreases with increasing scattering angle until it reaches the lower limiting value of around -0.5 at $\theta = 180°$. It is a general feature that for forward scattering angles $\boldsymbol{j}'$ tends to be weakly polarized along $\boldsymbol{k}$, whilst for backward scattering angles it is aligned strongly perpendicularly to $\boldsymbol{k}$.

The $\rho_{1+}^{\{2\}}(\theta)$ renormalized CC QM PDDCS measures the alignment of $\boldsymbol{j}'$ with respect to the $x + z$ or $x - z$ axes, while the $\rho_{2+}^{\{2\}}(\theta)$ renormalized PDDCSs measures the alignment of $\boldsymbol{j}'$ with respect to the x or y axes. At $\theta = 0°$ and 180°, both $\rho_{1+}^{\{2\}}(\theta)$ and $\rho_{2+}^{\{2\}}(\theta)$ must be zero, since the zx plane is then undefined. As the scattering angle is increased, $\rho_{1+}^{\{2\}}(\theta)$ passes through a maximum positive value, indicating that the rotational angular momentum is preferentially aligned parallel to $x + z$ axis. $\rho_{2+}^{\{2\}}(\theta)$, on the other hand, is generally found to be negative for most scattering angles, consistent with $\boldsymbol{j}'$ alignment preferentially along the y axis, *i.e.* out of the scattering plane.

2. Comparison of the HEHS, QCT, and QM renormalized PDDCS

Fig. 4 also compares the Λ-doublet state averaged CC QM renormalized PDDCSs with those obtained from the QCT and HEHS Monte Carlo calculations. In general, the CC QM, QCT, and HEHS alignment renormalized PDDCSs are in remarkably good agreement with each other in the classically allowed region. Note that the classical PDDCSs go to zero in the classically forbidden region, where the DCSs are also zero. At small scattering angles the HEHS and QCT renormalized PDDCSs are free from oscillations for all Δj, consistent with the latter having a quantum mechanical origin.

The fact that the CC QM renormalized PDDCSs are in such good agreement with the classical calculations suggests that, apart from the sharp diffraction structure at small scattering angles, the alignment of the NO(X) after collision is largely determined by a classical mechanism. Furthermore, the rotational alignment must be largely the result of impulsive forces, with attractive forces playing a very minor role in determining the alignment in the classical allowed scattering region. It is significant that both the Λ-doublet resolved and averaged renormalized PDDCSs shown in Figs. 3 and 4 vary relatively little with Δj, in sharp contrast to the DCSs. The value taken by the renormalized PDDCSs is dictated principally by the scattering angle, and not by the specific Δj. We return to the origin of this behavior at the end of the paper, in section III C 4.

3. Comparison of the HEHS QCT, QM rank 2 alignment parameters

Fig. 5 compares the scattering angle integrated polarization parameters, $a_{q\pm}^{\{k\}}$, obtained from the Λ-doublet averaged CC QM calculations with those from the QCT and HEHS calculations. The general trends in the alignment parameters as a function of Δj are similar to those of the corresponding renormalized PDDCS as a function of the scattering angle. This arises from the fact that the DCS becomes more backward scattered as j' increases, hence the more backward scattered region of the renormalized PDDCS makes a larger contribution to the final value of the alignment parameters.

The $a_0^{\{2\}}$ parameters become more negative as j' increases. For low j', the value of around +0.2 indicates parallel alignment of $\boldsymbol{j}'$ with respect to the initial relative velocity vector. Note that for $j' = 1.5$, the maximum value of the QM $a_0^{\{2\}}$ parameter is less than +0.45. As

Δj increases, the $a_0^{\{2\}}$ moment steadily decreases close to its limiting value of around -0.5, corresponding to an increasing degree of perpendicular alignment with respect to the initial relative velocity vector. Apart from some small differences, the $a_0^{\{2\}}$ heteronuclear hard shell alignment parameters are generally in good agreement with the CC QM and QCT parameters. As seen from the middle panel of Fig. 5, at low Δj the HEHS $a_{1+}^{\{2\}}$ parameters show observable deviations from both the Λ-doublet averaged QM and the QCT parameters. The $a_0^{\{2\}}$ and $a_{2+}^{\{2\}}$ alignment parameters from HEHS, QM, and averaged CC QCT data are generally in better agreement than for the $a_{1+}^{\{2\}}$ moment. The fact that the CC QM and QCT data sets are generally in good agreement with each other suggests that the failings of the HEHS model for the $a_{1+}^{\{2\}}$ moment are due to the neglect of attractive and 'soft repulsive' features in the potential, possibly due to the influence of chattering collisions,[17] rather than to a failure of classical mechanics.

Overall, the data presented in Fig. 5 provides support for the view that the rotational angular momentum alignment in the NO(X) + Ar system is mainly classical in origin. Furthermore, the alignment is seen to be largely imposed by impulsive forces, particularly for moderate to large changes in Δj.

4. 'Hybrid' QCT-QM alignment parameters

It has been shown in previous sections that the HEHS and QCT alignment parameters and renormalized PDDCSs reproduce well the Λ-doublet averaged CC QM data. However, as shown in Fig. 6, the Λ-doublet resolved open shell QM alignment parameters display oscillatory behavior as a function of Δj, which the (closed shell) QCT and HEHS calculations are unable to recover. Note that in the case of closed-shell QM calculations, an alternation depending on the parity (even/odd j' numbers) is observed.

The origin of the oscillations in the open shell data could either lie in differences in the CC QM DCSs or in the polarization behavior itself, as reflected in the renormalized PDDCSs. In order to trace back the origin of the oscillations in the $a_{q\pm}^{\{k\}}$ parameters, it is helpful to introduce 'hybrid' alignment parameters, defined according to the equation

$$a_{q\pm}^{\{k\},\mathrm{hibr}}(j\epsilon \to j'\epsilon') = \int_{-1}^{+1} (\mathrm{d}\cos\theta)\rho_{q\pm}^{\{k\},\mathrm{QCT}}(\theta; j \to j') \times \left[\frac{2\pi}{\sigma^{\mathrm{QM}}(j\epsilon \to j'\epsilon')}\frac{\mathrm{d}\sigma^{\mathrm{QM}}(\theta; j\epsilon \to j'\epsilon')}{\mathrm{d}\omega}\right] \qquad (11)$$

where the term in square brackets is the normalized QM DCS for the $j\epsilon \rightarrow j'\epsilon'$ transition and $\rho_{q\pm}^{\{k\},\mathrm{QCT}}(\theta; j \rightarrow j')$ is the QCT renormalized PDDCS for the $j \rightarrow j'$ transition. In this way, it is possible to calculate alignment parameters corresponding to a hypothetical scattering event, in which the alignment is due to classical behavior, while the DCS is shaped by quantum mechanics. In Fig. 6, the 'hybrid' QCT-QM alignment parameters are plotted along with the exact open shell QM alignment parameters. As can be seen, both the trend and the parity dependent quantum mechanical oscillations are reproduced well by the hybrid data. This figure demonstrates that fundamentally, even at the level of Λ-doublet state resolution, the rotational alignment of the NO(X) after collision has a classical origin.

Fig. 7 elucidates the origin of the agreement seen in the alignment parameters determined using the 'hybrid' model and the exact CC QM calculations. In the upper panel, the renormalized PDDCSs for the open shell CC QM $\Delta j = 10$, $f \rightarrow f/e$ transitions and for the (closed shell) QCT $\Delta j = 10$ transition are compared. At low scattering angles, the renormalized CC QM PDDCS for the parity conserving transition is somewhat more positive than for the parity changing collision, but they become virtually identical in the backward scattered region. The QCT renormalized PDDCS lies between the two QM ones, and is roughly the average of the two. At large scattering angles the three renormalized PDDCSs are almost identical. Even at the level of parity resolved collisions, the quantum mechanical renormalized PDDCSs can be estimated reasonably using the quasi-classical ones without serious loss of accuracy.

In contrast, the open shell CC QM normalized DCSs are very different for the parity changing and parity conserving transitions, as shown in the middle panel of Fig. 7 (the corresponding HEHS and QCT DCSs were shown in Fig. 2). The parity changing normalized DCS has a broad single peak centered around 60°, while that of the parity conserving transition comprises of two peaks having maxima at 30° and 100°.[11–13] As noted previously, it has been suggested that this parity dependent behavior of the DCSs arises from quantum mechanical interference between alternative pathways scattered from the different ends and the flatter sides of the molecule.[11–13] The normalized PDDCS is the product of the renormalized PDDCS and the normalized DCS (*i.e.* the product of the data shown in the upper panel and the middle panel of Fig. 7). In the bottom panel of Fig. 7 the exact open shell CC QM normalized PDDCSs are shown, as obtained by multiplying the QM renormalized PDDCSs and the normalized QM DCSs, along with the 'hybrid' PDDCS, *i.e.* the product

of the QCT renormalized PDDCS and the normalized QM DCSs. As seen from Fig. 7, the 'hybrid' and CC QM PDDCSs are very similar for both the parity changing and conserving transitions. Given that the alignment parameters are simply the integral of the normalized PDDCSs over the all scattering angles, the difference between the alignment parameters for different Λ-doublet levels arises primarily from the differences between the two corresponding quantum mechanical DCSs. The rotational alignment behavior itself can be described remarkably well by classical mechanics.

C. Conservation of the projection of j' on the kinematic apse

1. Rotation to the apse frame

It is helpful at this point to recall the definition of the *kinematic apse*, $\hat{\boldsymbol{a}}$, given in Eq. (3). Classically, it is well known that the component of the angular momentum along the kinematic apse is rigorously conserved for impulsive collisions, such as those involved in the classical HOHS and HEHS calculations already presented.[20] The agreement between the HEHS results and those from the CC QM and QCT calculations suggests that impulsive forces are largely responsible for the observed alignment behavior. Classically, one would therefore expect the projection of $\boldsymbol{j}$ along the kinematic apse to be conserved, as is indeed largely the case for all but the most forward scattered, low Δj collisions.[20]

In order to test the extent to which the kinematic apse model holds true quantum mechanically one has to rotate the scattering density matrix of Eq. (7) into a frame in which the kinematic apse is the quantization axis. For this purpose we define the apse frame, which has its z-axis along $\hat{\boldsymbol{a}}$, and the scattering plane lying in the zx plane. In this case, the axis of quantization, *i.e.* the new z-axis, is the kinematic apse rather than the initial relative velocity axis, $\boldsymbol{k}$. The (complex) renormalized PDDCS can be rotated into the apse frame using the Wigner rotation matrices according to the equation[27]

$$\rho_q^{(k),\hat{\boldsymbol{a}}}(\theta) = \sum_p D_{pq}^{(k)}(0,\beta,0)\,\rho_p^{(k)}(\theta) = \sum_p d_{pq}^{(k)}(\beta)\,\rho_p^{(k)}(\theta)\,, \tag{12}$$

where the superscript $\hat{\boldsymbol{a}}$ indicates that the renormalized PDDCS is given in the apse frame, and β is the angle between $\hat{\boldsymbol{a}}$ and $\hat{\boldsymbol{k}}$ and is a function of the scattering angle

Fig. 8 compares the scattering frame PDDCSs with those in the apse frame, as obtained though application of Eq. (12). The figure shows the renormalized CC QM PDDCS for

the $\Delta j = 10$, $f \rightarrow f$ transition in the scattering frame and the apse frame for spin-orbit conserving and spin-orbit changing transitions. Whilst the scattering frame $\rho_0^{\{2\}}(\theta)$ PDDCSs vary significantly with scattering angle (left panels), the corresponding apse frame PDDCSs (right panels) are almost constant with a value close to -0.5, except for forward scattering angles. This indicates a near maximum alignment of $\boldsymbol{j}'$ perpendicular to the kinematic apse. Similarly, whilst the scattering frame $\rho_{1+}^{\{2\}}(\theta)$ and $\rho_{2+}^{\{2+\}}(\theta)$ renormalized PDDCSs vary significantly with scattering angle, in the apse frame, apart from in the most forward scattered region, both parameters take near constant values of around zero.

The scattering frame alignment parameters (presented in Fig. 5 and section III C 2) can be compared with the apse frame alignment parameters, as displayed in Fig. 9. Once more, while the scattering frame alignment parameters show significant variation with Δj, when rotated into the apse frame they too display near-constant values independent of Δj. The apse frame $a_0^{\{2\}}$ parameters are all close to the lower limiting value of around -0.5, confirming perpendicular alignment of $\boldsymbol{j}'$ with respect to the kinematic apse. The other two second rank components, $a_{1+}^{\{2\}}$ and $a_{2+}^{\{2\}}$, oscillate around zero in the apse frame. The apse frame QM polarization parameters suggest that, at least as far as the rank $k = 2$ moments are concerned, $\boldsymbol{j}'$ is cylindrically distributed near perpendicularly to the kinematic apse, as is consistent with apse model discussed below. It is worth noting that the parity dependent oscillations visible in the scattering frame for all three parameters have smaller amplitudes in the apse frame, and in the case of $a_0^{\{2\}}$ the oscillations practically disappear. This reinforces the conclusions of the preceding section, that the angular momentum alignment has a common (essentially classical) dynamical origin, whilst the oscillatory structure in the alignment parameters reflects the quantum mechanical structure in the parity resolved DCSs.

The behavior of the spin-orbit conserving and spin-orbit changing collisions is remarkably similar (compare the upper and lower rows of Fig. 8 and Fig. 9). In the Hund's case (a) limit, recall that spin-orbit changing collisions take place on the V_{diff} potential, which is considerably more attractive than V_{sum}.[8] This is reflected in the alignment parameters in the apse frame, which tend to take the constant values seen for the spin-orbit conserving transitions only at higher Δj values. Nevertheless, the similarities between the alignment parameters shown in the upper and lower panels of Fig. 9 are striking, particularly once the data are transformed into the apse frame.

2. The effect of the collision energy on the alignment behavior

As discussed in section III B, the polarization parameters,[25] $a_{q\pm}^{\{k\}}$, are given by the integral of the normalized PDDCSs over the whole scattering angle region; that is the integral of the renormalized PDDCS multiplied by the normalized differential cross section. Depending on the final state and the collision energy, different DCSs and PDDCSs determine the final value of the alignment parameters. If the collision energy is comparable to the attractive well on the interaction potential, the presence of strong quantum interferences are expected to appear in the scattering dynamics. The renormalized apse frame PDDCSs obtained at a collision energy of $E_{\rm coll} = 15\,$meV are compared with those obtained at $E_{\rm coll} = 66\,$meV in Fig. 10, while Fig. 11 compares the apse frame alignment parameters at $E_{\rm coll} = 15$, 30 and 66 meV.

The apse frame renormalized (k=2, q=0) PDDCSs for $\Delta j = 3$, 7 and 10 are shown in the lowest panel of Fig. 10. Specifically, at low collision energy, 15 meV, the respective renormalized PDDCSs for $\Delta j = 3$ and 7 deviate significantly from the value of -0.5 predicted by the kinematic apse model. They also show strong scattering angle dependent oscillatory behavior, which becomes increasingly confined to the forward scattered region as the collision energy is raised. The apse frame $\rho_0^{\{2\}}(\theta)$ moments at 66 meV show a sharp peak at small scattering angles, but drop quickly down to the lower limit with increasing scattering angle. Note that the corresponding DCSs, shown in the upper panel of Fig. 10, are generally strongly forward peaked, particularly at low Δj, and thus this region makes the most contribution to the final values of the alignment parameters, which are shown in Fig. 11. There is no well-defined trend exhibited by the $a_{1+}^{\{2\}}$ and $a_{2+}^{\{2\}}$ alignment parameters with Δj at a collision energy of $E_{\rm coll} = 15\,$meV. However, the apse frame $a_{1+}^{\{2\}}$ and $a_{2+}^{\{2\}}$ parameters deviate observably from the zero values expected from the apse model introduced below, particularly for low Δj transitions. As the collision energy is raised, the collisions become more impulsive, dominated by the repulsive core of the potential, and $\boldsymbol{j}'$ becomes progressively more aligned perpendicular to the kinematic apse. Collisions leading to high Δj are also more impulsive, and the $a_0^{\{2\}}$ parameters approach their lower limiting value. In addition, in the apse frame the $a_{1+}^{\{2\}}$ and $a_{2+}^{\{2\}}$ parameters tend to take values increasingly close to zero as the collision energy is raised.

3. Magnetic level populations in the apse frame resolved in scattering angle

The diagonal elements of the density matrix represent the populations in the different $m_{j'}$ states belonging to a particular j'. Given that initially NO(X) is in its rotational ground state, $j = 0.5$, only the $m_j = \pm 0.5$ states are initially populated, regardless of the choice of quantization axis. If preferential population of $m_{j'} = \pm 0.5$ states were observed, this would therefore suggest that the projection of $\boldsymbol{j}$ along a given axis is conserved.

The upper panels of Fig. 12 show the scattering $m_{j'}$ and apse frame $m_{j'}^{\hat{\boldsymbol{a}}}$ populations as a function of scattering angle for the $|1/2, 0.5, -1\rangle \rightarrow |1/2, 10.5, -1\rangle$ transitions at a collision energy of 66 meV. The scattering frame and apse frame populations differ considerably, as seen from the top two panels of the figure. At 0° and 180° only the ± 0.5 states are occupied in both frames, as at these scattering angles the $\boldsymbol{k}$, $\boldsymbol{k}'$ and $\boldsymbol{a}$ axes all coincide except for a possible change of sign. The final rotational angular momentum is kinematically constrained to negative alignment with respect to $\boldsymbol{k}$ as well as to $\boldsymbol{k}'$ in the limits of forward and backward scattering. As the scattering angle increases, the population shifts to low $m_{j'}$ values in the scattering frame, and the $m_{j'} = \pm 0.5$ states become the only significantly occupied ones at scattering angles greater than 150°. In the apse frame (top right panel), high $m_{j'}^{\hat{\boldsymbol{a}}}$ states are only populated in the very forward scattered region ($\theta \lesssim 15°$), with the lowest $m_{j'}^{\hat{\boldsymbol{a}}}$ levels tending to become populated at scattering angles $\theta \gtrsim 15°$. In the lower panels of Fig. 12, the diagonal elements of the apse frame density matrix, *i.e.* the $m_{j'}^{\hat{\boldsymbol{a}}}$ populations, are plotted as a function of scattering angle for the $|1/2, 0.5, -1\rangle \rightarrow |1/2, 5.5, -1\rangle$ transition at collision energies of 15 meV and 66 meV. Notice that at the lower collision energy (lower left panel), the $m_{j'}^{\hat{\boldsymbol{a}}}$ populations are less peaked at $m_{j'}^{\hat{\boldsymbol{a}}} = \pm 1/2$.

These observations confirm that quantum mechanically the kinematic apse model largely holds true for NO(X) + Ar at collision energies of 66 meV for all but the most forward scattering angles. $m_{j'}^{\hat{\boldsymbol{a}}}$ becomes increasingly conserved as j' increases (compare the upper and lower right hand panels of Fig. 12). These collisions can be characterized as being impulsive since the depth of the attractive well, which is about 10 meV, is much less than the collision energy. When the collision energy is reduced to 15 meV, only a weak propensity for the $m_j^{\hat{\boldsymbol{a}}}$ conserving transitions can be observed, as shown for the $j' = 5.5$ transition in the bottom left panel of Fig. 12. In this case, attractive forces cannot be neglected in the interaction between NO(X) and Ar.

The above discussion ignores coherent population of different $m_{j'}^{\hat{\boldsymbol{a}}}$ states, *i.e.* off-diagonal elements of the density matrix. However, the fact that the kinematic apse frame renormalized $(k, q\pm) = (2,1+)$ and $(2,2+)$ PDDCSs and alignment parameters shown in the right panels of Fig. 8 average to zero suggests that the $k = 2$ off-diagonal elements of the apse-frame density matrix do not contribute significantly to the scattering dynamics.

4. The kinematic apse model

In the kinematic apse model (AM) we assume that the projection of $\boldsymbol{j}'$ onto the kinematic apse is conserved, and only the $m_{j'}^{\hat{\boldsymbol{a}}} = \pm 0.5$ states are populated after the collision. In addition, as explained elsewhere,[19] coherences between the $m_{j'}^{\hat{\boldsymbol{a}}} = \pm 0.5$ states do not affect polarization moments of even rank. So, for the purpose of this paper – calculation of rank 2 PDDCSs and alignment parameters – we can set all off-diagonal elements to zero, which is equivalent to imposing cylindrical symmetry on the $\boldsymbol{j}'$ distribution about the kinematic apse. In this case, only the $\langle j'+0.5|\rho(\theta)|j'+0.5\rangle = \langle j'-0.5|\rho(\theta)|j'-0.5\rangle$ elements of the apse frame density matrix are non-zero, and, as a consequence, the scattering frame Hertel-Stoll renormalized PDDCSs within the apse model, $\rho_0^{\{k\}\mathrm{AM}}(\theta)$, can be expressed as a product of Clebsch-Gordon coefficients and $d^k_{qq'}(\cdots)$ rotation matrix elements (see Appendix):

$$\rho_0^{\{k\}\mathrm{AM}}(\theta) = \frac{1}{2}\left[1+(-1)^k\right]\, d^k_{00}(-\beta)\langle j'\tfrac{1}{2}, k\,0|j'\tfrac{1}{2}\rangle \qquad q=0 \tag{13}$$

$$\rho_{q+}^{\{k\}\mathrm{AM}}(\theta) = (-1)^q\frac{1}{\sqrt{2}}\left[1+(-1)^k\right]\, d^k_{0q}(-\beta)\langle j'\tfrac{1}{2}, k\,0|j'\tfrac{1}{2}\rangle \qquad q>0\,,$$

and $\rho_{q-}^{\{k\}\mathrm{AM}}(\theta) = 0$. Clearly, the $k =$ odd PDDCSs and polarization parameters vanish, and hence no orientation information can be gained in either the scattering frame or the apse frame when the apse model is applied.

In the case of a closed shell molecule, the apse model assumes that $\boldsymbol{j}'$ is perfectly aligned perpendicular to the kinematic apse, but shows no orientation or alignment with respect to the remaining axes. In this case, only the even k, $q = 0$ renormalized PDDCSs and polarization parameters are non-zero in the apse frame. The renormalized PDDCSs predicted by the apse model are shown in Fig. 13, where they are plotted in the scattering frame. Note that the effect of rotation from the apse to the scattering frame is to mix the PDDCSs of the same k but different q. The heteronuclear hard shell and apse model renormalized PDDCS are identical in the classically allowed region. In general, the agreement between

the quantum mechanical and apse model renormalized PDDCSs is very good, although the apse model PDDCSs do not show QM oscillations in the forward scattered region, or parity dependent undulations in the side-ways or backward scattered region. The largest deviation is observed at low scattering angles, where attractive forces have the greatest influence on the collision dynamics. At higher scattering angles, the QM and apse model PDDCSs become almost identical. Interestingly, for $\Delta j = 14$, the deviation between the apse and full QM treatments is more pronounced than that for $\Delta j = 10$ and $\Delta j = 3$, although it should be borne in mind that the DCSs for the high j' states are more confined to the backward scattered region, where the agreement is better.

Given the PDDCS data shown in Fig. 13, it is perhaps not surprising that the CC QM and apse model alignment parameters (not shown) are also in very good agreement. In the apse frame, the apse model $a_0^{\{2\}\mathrm{AM}}$ parameters take their lowest possible value, close to -0.5, and the apse frame QM parameters, $a_0^{\{2\}}$, are close to this value for most j' states, particularly in the case of spin-orbit conserving transitions, as was shown in the top panel of Fig. 9. For low Δj, the apse frame QM $a_0^{\{2\}}$ alignment parameters tend to be somewhat less negative than the AM limiting value, reflecting the fact that the interaction between the NO(X) and Ar cannot be characterized as purely impulsive for these collisions. For this reason, at low Δj, $\boldsymbol{j}'$ is not necessarily exactly aligned perpendicular to the apse axis. However, for high Δj the agreement between the apse model and the QM calculations is excellent. Fig. 9 also shows that for all j' states the CC QM apse frame $a_{1+,}^{\{2\}}$ and $a_{2+}^{\{2\}}$ parameters are both close to the zero value predicted by the apse model. Although the discrepancy between the apse frame CC QM and apse model $a_{2+}^{\{2\}\mathrm{AM}}$ parameters is somewhat greater than for the other parameters, comparing the observed values to the limits[47] of these parameters reveals that no significant alignment of $\boldsymbol{j}'$ is present, apart from that with respect to the kinematic apse.

Finally, in section III B 2 it was noted that the renormalized PDDCSs shown in Figs. 3 and 4 all showed very similar dependencies as a function of scattering angle. The reason for this is now clear. In the apse frame, the renormalized PDDCSs at 66 meV take near constant values, independent of scattering angle. The angular dependence observed in the scattering frame simply reflects the apse-to-scattering frame coordinate transformation, and specifically the angular dependence of the $k = 2$ reduced rotation matrix elements, $d_{pq}^k(\beta)$, appearing in Eq. (13). On the other hand, if the collision energy is not high enough to render the collision an impulsive one, the apse model provides a less reliable approximation.

IV. CONCLUSIONS

This paper represents the first part of an investigation into the polarization effects in the collisions of ground state NO(X) and argon, focussing on the origin of collision-induced rotational alignment. The quantum mechanical Λ-doublet resolved renormalized PDDCSs were characterized, and show no significant differences between transitions which conserve or change the NO(X) parity. However, the corresponding (integrated) second rank alignment parameters exhibit strong parity dependent oscillations as a function of the final rotational state.

By comparing the averaged CC QM, QCT, and heteronuclear hard shell PDDCSs and alignment parameters it has been shown that the dynamics leading to the observed rotational angular momentum alignment is primarily classical in behavior. At the collision energy of 66 meV, the hard shell nature of the ground state NO(X) is mainly responsible for the rotational alignment of the NO(X) molecule. In contrast, the parity dependent oscillations of the alignment parameters as a function of the final rotational and Λ-doublet level arises from the differences in the shape of differential cross sections. The latter in turn originate from quantum mechanical interferences, as described in previous work,[11–13] which are not manifest in the QM rotational alignment. This suggests that the rotational alignment and the DCSs are sensitive to rather different aspects of the scattering dynamics.

The applicability of the kinematic apse model was also tested quantum mechanically. It was shown to be a good assumption under the conditions of typical crossed molecular beam experiments on this system. However, the extent to which the projection of the rotational angular momentum onto the kinematic apse is conserved depends on the collision energy and on the final rotational state. It would be interesting to see how ubiquitous the impulsive alignment mechanism is in other inelastic and reactive scattering processes.

In the accompanying paper, the behavior described here theoretically will be confirmed through experimental measurement of the collision induced angular momentum alignment at the fully quantum state resolved level.[24]

Acknowledgements

The support from EPSRC (*via* Programme Grant No. EP/G00224X/1) and the EU (*via* FP7 EU People ITN project 238671) to M.B. is gratefully acknowledged. FJA and PGJ

acknowledge the financial support by the Spanish Ministry of Education and Science under the grant CTQ2008-02578/BQU and Consolider Ingenio 2010 CSD2009-00038. B.H. was funded by the ITN7 Marie Curie Actions grant (project 238671) as a member of the ICONIC network. S.S. acknowledges support from the National Natural Science Foundation of China under Grant No. 11034003, and the National Basic Research Program of China under Grant No. 2013CB922200.

Appendix: Renormalized PDDCS according to the kinematic apse model

In the framework of the apse model there are only two non-zero apse frame density matrix elements, independent of scattering angle, namely $\langle j'\frac{1}{2}|\rho(\theta)|j'\frac{1}{2}\rangle = \langle j'-\frac{1}{2}|\rho(\theta)|j'-\frac{1}{2}\rangle = \frac{1}{2}$. Off-diagonal elements, of the form $\langle j'\frac{1}{2}|\rho(\theta)|j'-\frac{1}{2}\rangle$, arising from coherent population of $m^a_{j'}$ states, are assumed to be zero within the model. The apse frame renormalized PDDCSs thus can be expressed in terms of Clebsch–Gordan coefficients:

$$\begin{aligned}\rho_q^{(k),\hat{\boldsymbol{a}}} &= \sum_{m_1^a,m_2^a} \langle j'm_1^a|\rho(\theta)|j'm_2^a\rangle\langle j'm_1^a, kq|j'm_2^a\rangle \\ &= \langle j'\tfrac{1}{2}|\rho(\theta)|j'\tfrac{1}{2}\rangle\langle j'\tfrac{1}{2}, k0|j'\tfrac{1}{2}\rangle + \langle j'-\tfrac{1}{2}|\rho(\theta)|j'-\tfrac{1}{2}\rangle\langle j'-\tfrac{1}{2}, k0|j'-\tfrac{1}{2}\rangle \\ &= \frac{1}{2}\left[\langle j'\tfrac{1}{2}, k0|j'\tfrac{1}{2}\rangle + \langle j'-\tfrac{1}{2}, k0|j'-\tfrac{1}{2}\rangle\right] \\ &= \frac{1}{2}\left[1+(-1)^k\right]\langle j'\tfrac{1}{2}, k0|j'\tfrac{1}{2}\rangle\end{aligned} \tag{A.1}$$

Note that only the even k, $q = 0$ renormalized PDDCSs are non-zero in the apse frame. The apse model is therefore equivalent to assuming that $\boldsymbol{j'}$ lies perpendicular to the kinematic apse, with cylindrical symmetry about it. Similar expressions hold for the integrated polarization parameters, $a_q^{(k),\hat{\boldsymbol{a}}}$, in the apse frame. These parameters have to be transformed into the scattering frame from the apse frame, which is achieved by a clockwise rotation about the y-axis of the scattering frame by the apse angle β. When invoking the Hertel-Stoll normalization, given by Eq. (9), one has for $q = 0$:

$$\begin{aligned}\rho_0^{\{k\}\mathrm{AM}}(\theta) &= d^k_{00}(-\beta)\,\rho_0^{\{k\},\hat{\boldsymbol{a}}} \\ &= \frac{1}{2}\left[1+(-1)^k\right] d^k_{00}(-\beta)\,\langle j'\tfrac{1}{2}, k0|j'\tfrac{1}{2}\rangle\end{aligned} \tag{A.2}$$

and for $q > 0$:

$$\begin{aligned}
\rho_{q+}^{\{k\}\mathrm{AM}}(\theta) &= \frac{1}{\sqrt{2}}\left[(-1)^q \rho_{+q}^{(k)}(\theta) + \rho_{-q}^{(k)}(\theta)\right] \\
&= \frac{1}{\sqrt{2}}\left[(-1)^q \rho_0^{(k),\hat{\boldsymbol{a}}}(\theta) d_{0q}^k(-\beta) + \rho_0^{(k),\hat{\boldsymbol{a}}}(\theta) d_{0-q}^k(-\beta)\right] \\
&= (-1)^q \sqrt{2} d_{0q}^k(-\beta)\, \rho_0^{(k),\hat{\boldsymbol{a}}}(\theta) \\
&= (-1)^q \frac{1}{\sqrt{2}}\left[1 + (-1)^k\right] d_{0q}^k(-\beta)\, \langle j' \tfrac{1}{2}, k0 | j' \tfrac{1}{2}\rangle\,, \qquad \text{(A.3)}
\end{aligned}$$

and

$$\rho_{q-}^{\{k\}\mathrm{AM}}(\theta) = 0\,, \qquad \text{(A.4)}$$

which are in agreement with the equations given in section III C.

REFERENCES

[1] D. A. Case and D. R. Herschbach, Mol. Phys. **30**, 1537 (1975).

[2] D. A. Case, G. M. McClelland, and D. R. Herschbach, Mol. Phys. **35**, 541 (1978).

[3] F. J. Aoiz, M. Brouard, and P. A. Enriquez, J. Chem. Phys. **105**, 4964 (1996).

[4] M. P. de Miranda and D. C. Clary, J. Chem. Phys. **106**, 4509 (1997).

[5] M. H. Alexander, J. Chem. Phys. **76**, 5974 (1982).

[6] M. H. Alexander, Chem. Phys. **92**, 337 (1985).

[7] M. H. Alexander, P. Andresen, R. Bacis, R. Bersohn, F. J. Comes, P. J. Dagdigian, R. N. Dixon, R. W. Field, G. W. Flynn, K.-H. Gericke, E. R. Grant, B. J. Howard, J. R. Huber, D. S. King, J. L. Kinsey, K. Kleinermanns, K. Kuchitsu, A. Luntz, A. J. McCaffery, B. Pouilly, H. Reisler, S. Rosenwacks, E. W. Rothe, M. Shapiro, J. P. Simons, R. Vasudev, J. R. Wiesenfeld, C. Wittig, and R. N. Zare, J. Chem. Phys. **89**, 1749 (1988).

[8] M. H. Alexander, J. Chem. Phys. **111**, 7426 (1999).

[9] Y. Sumiyoshi and Y. Endo, Mol. Phys. **127**, 184309 (2007).

[10] F. J. Aoiz, J. E. Verdasco, V. J. Herrero, V. S. Rábanos, and M. H. Alexander, J. Chem. Phys. **119**, 5860 (2003).

[11] C. J. Eyles, M. Brouard, C.-H. Yang, J. Kłos, F. J. Aoiz, A. Gijsbertsen, A. E. Wiskerke, and S. Stolte, Nature Chemistry **3**, 597 (2011).

[12]C. J. Eyles, M. Brouard, H. Chadwick, B. Hornung, B. Nichols, C.-H. Yang, J. Kłos, F. J. Aoiz, A. Gijsbertsen, A. E. Wiskerke, and S. Stolte, Phys. Chem. Chem. Phys. **14**, 5403 (2012).

[13]C. J. Eyles, M. Brouard, H. Chadwick, F. J. Aoiz, J. Kłos, A. Gijsbertsen, X. Zhang, and S. Stolte, Phys. Chem. Chem. Phys. **14**, 5420 (2012).

[14]J. I. Cline, K. T. Lorenz, E. A. Wade, J. W. Barr, and D. W. Chandler, J. Chem. Phys. **115**, 6277 (2001).

[15]E. A. Wade, K. T. Lorenz, D. W. Chandler, J. W. Barr, and G. L. Barnes, Chem. Phys. **301**, 261 (2004).

[16]M. H. Alexander, J. Chem. Phys. **99**, 7725 (1993).

[17]F. J. Aoiz, J. E. Verdasco, V. J. Herrero, and V. S. Rábanos, Phys. Chem. Chem. Phys. **6**, 4407 (2004).

[18]M. Lemeshko and B. Friedrich, Phys. Rev. A **79**, 12718 (2009).

[19]P. Jambrina, J. Kłos, F. Aoiz, and M. de Miranda, Phys. Chem. Chem. Phys. **14**, 9826 (2012).

[20]V. Khare, D. J. Kouri, and D. K. Hoffman, J. Chem. Phys. **74**, 2275 (1981).

[21]D. K. Hoffman, J. W. Evans, and D. J. Kouri, J. Chem. Phys. **80**, 144 (1984).

[22]Y. Kim and H. Meyer, Chem. Phys. **301**, 273 (2004).

[23]A. Gijsbertsen, H. V. Linnartz, C. A. Taatjes, and S. Stolte, J. Am. Chem. Soc. **128**, 8777 (2006).

[24]M. Brouard, H. Chadwick, C. J. Eyles, B. Hornung, B. Nichols, F. J. Aoiz, P. G. Jambrina, and S. Stolte, J. Chem. Phys. **xxx**, xxxx (2012).

[25]M. P. de Miranda, F. J. Aoiz, L. Bañares, and V. S. Rábanos, J. Chem. Phys **111**, 5368 (1999).

[26]N. E. Shafer-Ray, A. J. Orr-Ewing, and R. N. Zare, J. Phys. Chem. **99**, 7591 (1995).

[27]R. N. Zare, *Angular Momentum, Understanding Spatial Aspects in Chemistry and Physics* (John Wiley and Sons, New York, 1988).

[28]I. V. Hertel and W. Stoll, Adv. At. Mol. Phys. **13**, 113 (1977).

[29]HIBRIDON is a package of programs for the time-independent quantum treatment of inelastic collisions and photodissociation written by M. H. Alexander, D. Manolopoulos, H.-J. Werner, and B. Follmeg, with contributions by P. F. Vohralik, D. Lemoine, G. Corey, R. Gordon, B. Johnson, T. Orlikowski, A. Berning, A. Degli-Esposti, C. Rist, P. Dagdigian,

B. Pouilly, G. van der Sanden, M. Yang, F. de Weerd, S. Gregurick, and J. Kłos.

[30]D. E. Manolopoulos, J. Chem. Phys. **85**, 6425 (1986).

[31]M. H. Alexander and D. E. Manolopoulos, J. Chem. Phys. **86**, 2044 (1987).

[32]M. J. L. de Lange, M. Drabbels, P. T. Griffiths, J. Bulthuis, S. Stolte, and J. G. Snijders, Chem. Phys. Lett. **313**, 491 (1999).

[33]K. T. Lorenz, D. W. Chandler, J. W. Barr, W. Chen, G. L. Barnes, and J. L. Cline, Science **293**, 2063 (2001).

[34]J. Z. H. Zhang and W. H. Miller, J. Chem. Phys. **91**, 1528 (1989).

[35]J. Aldegunde, M. P. de Miranda, J. M. Haigh, B. K. Kendrick, V. Sáez-Rábanos, and F. J. Aoiz, J. Phys. Chem. A **109**, 6200 (2005).

[36]F. J. Aoiz, L. Bañares, and V. J. Herrero, J. Chem. Soc. Faraday Trans. **94**, 2483 (1998).

[37]R. A. Budde and R. B. Bernstein, J. Chem. Phys. **55**, 5499 (1971).

[38]D. Beck and U. Ross, Z. Phys. **293**, 541 (1979).

[39]T. G. Kreutz and G. W. Flynn, J. Chem. Phys. **93**, 452 (1990).

[40]P. C. Jurs, *Computer Software Applications in Chemistry* (Wiley-Interscience, New York, 1986).

[41]H. J. Korsch and R. Schinke, J. Chem. Phys. **73**, 1222 (1980).

[42]H. J. Korsch and R. Schinke, J. Chem. Phys. **75**, 3850 (1981).

[43]R. Schinke, Chem. Phys. **34**, 65 (1978).

[44]J. Kłos, F. J. Aoiz, J. E. Verdasco, M. Brouard, S. Marinakis, and S. Stolte, J. Chem. Phys. **127**, 031102 (2007).

[45]F. J. Aoiz, J. E. Verdasco, M. Brouard, J. Kłos, S. Marinakis, and S. Stolte, J. Phys. Chem. A **113**, 14636 (2009).

[46]A. Gijsbertsen, H. Linnartz, A. E. Wiskerke, S. Stolte, D. W. Chandler, and J. Kłos, J. Chem. Phys. **123**, 224305 (2005).

[47]J. Aldegunde, F. J. Aoiz, and M. P. de Miranda, Phys. Chem. Chem. Phys. **10**, 1139 (2008).

FIG. 1. Differential cross sections obtained from the (closed shell) classical homonuclear hard shell (HOHS - green continuous line) and heteronuclear hard shell (HEHS - blue dashed-dotted line) Monte Carlo calculations at a collision energy of 66 meV: $\Delta j = 3$ (top left); $\Delta j = 6$ (top right); $\Delta j = 10$ (bottom left); and $\Delta j = 14$ (bottom right). The homonuclear and heteronuclear IOS rainbow angles are marked with red cross-ended arrows and black square-ended arrows, respectively.

FIG. 2. Differential cross sections from the open-shell CC QM (black solid line), the QCT (red dashed line) and the heteronuclear hard shell (blue dashed-dotted line) calculations at a collision energy of 66 meV: $\Delta j = 3$ (top left); $\Delta j = 6$ (top right); $\Delta j = 10$ (bottom left); and $\Delta j = 14$ (bottom right). The open-shell CC QM data are for the spin-orbit conserving transitions, and have been averaged over initial and summed over final Λ-doublet state.

FIG. 3. Comparison of the scattering frame open shell CC QM DCSs and $k = 2$ renormalized PDDCSs for the transitions $j = 0.5, f \rightarrow j', f/e$. All the data are for spin-orbit conserving transitions from $\Omega = 1/2$. The black continuous lines show the data for NO(X) parity conserving transitions, whilst the red dashed lines are for NO(X) parity changing collisions. Note that parity conservation has a large effect on the DCSs, but only a small influence on the $k = 2$ alignment renormalized PDDCSs.

FIG. 4. Comparison of the scattering frame CC QM (black continuous line), quasi-classical (red dashed line), hard shell (blue dot-dashed line) second rank ($k = 2$) PDDCSs for $q = 0$ (top row), $q = 1+$ (middle row), $q = 2+$ (bottom row) for $\Delta j = 3$ (left column), 10 (middle column), and 14 (right column). All the data were obtained at a collision energy of 66 meV, and the open-shell CC QM data have been averaged over initial and summed over final Λ-doublet state.

FIG. 5. Comparison of the scattering frame CC QM (black open squares), QCT (red open circles), and heteronuclear hard shell (blue open triangles) second rank polarization parameters $q = 0$ (top panel), $q = 1+$ (middle panel), $q = 2+$ (bottom panel). All the data were obtained at a collision energy of 66 meV, and the open-shell CC QM data have been averaged over initial and summed over final Λ-doublet state.

FIG. 6. Comparison of the scattering frame second rank $k = 2$ alignment parameters, $a_0^{\{2\}}$ (top panel), $a_{1+}^{\{2\}}$ (middle panel), $a_{2+}^{\{2\}}$ (bottom panel), obtained from the CC QM (black open squares) and the 'hybrid' (red filled squares) calculations for the $|1/2, 0.5, f\rangle \rightarrow |1/2, j', f\rangle$ Λ-doublet resolved transitions. All the data were obtained at a collision energy of 66 meV. See text for details of the 'hybrid' calculations.

FIG. 7. Top panel: The scattering frame $|1/2, 0.5, f\rangle \rightarrow |1/2, 10.5, f(e)\rangle$ parity conserving (black solid line) and parity changing (red dashed line) CC QM, and QCT (blue dotted line) renormalized PDDCSs, $\rho_0^{\{2\}}(\theta)$. Middle panel: the parity conserving (black solid line) and parity changing (red dashed line) CC QM normalized DCSs (*i.e.* the angular distributions). Bottom panel: the corresponding parity conserving (black solid line) and parity changing (red dashed line) CC QM normalized PDDCS, and $n_0^{\{2\},\mathrm{hibr}} = \rho_0^{\{2\},\mathrm{QCT}} \times (2\pi/\sigma^{\mathrm{QM}})(\mathrm{d}\sigma^{\mathrm{QM}}/\mathrm{d}\omega)$, the 'hybrid' QCT/QM normalized PDDCS (green dotted and blue dashed-dotted lines). All the data were obtained at a collision energy of 66 meV.

FIG. 8. The CC QM renormalized PDDCSs in the scattering frame (left panels) and the apse frame (right panels) for the $\Delta j = 10$, $f \rightarrow f$, spin–orbit conserving (top row) and spin–orbit changing (bottom row) transitions: $\rho_0^{\{2\}}(\theta)$ (black solid line), $\rho_{1+}^{\{2\}}(\theta)$ (red dashed line), and $\rho_{2+}^{\{2\}}(\theta)$ (blue dashed-dotted line).

FIG. 9. The CC QM integrated alignment parameters in the apse frame for the Δj $f \rightarrow f$ spin-orbit conserving (top panel) and spin–orbit (bottom panel) changing transitions: $a_0^{\{2\},\hat{\boldsymbol{a}}}$ (black open squares), $a_{1+}^{\{2\},\hat{\boldsymbol{a}}}$ (red open circles), and $a_{2+}^{\{2\},\hat{\boldsymbol{a}}}$ (blue open triangles). All the data were obtained at a collision energy of 66 meV.

FIG. 10. Upper panels: The CC QM DCSs for the $\Delta j = 3$ (left), $\Delta j = 7$ (middle), $\Delta j = 10$ $f \rightarrow f$ spin–orbit conserving transitions at collision energies of 15 meV (black continuous line) and 66 meV (red dashed line). Lower panels: The apse frame renormalized CC QM PDDCSs, $\rho_0^{\{2\},\hat{\boldsymbol{a}}}$, for the $\Delta j = 3$ (left), $\Delta j = 7$ (middle), $\Delta j = 10$, $f \rightarrow f$ spin–orbit conserving transitions at collision energies of 15 meV (black continuous line) and 66 meV (red dashed line). Note that for 15 meV $\Delta j = 10$ is not accessible.

FIG. 11. The CC QM apse frame $k = 2$ alignment parameters, $a_0^{\{2\},\hat{\boldsymbol{a}}}$ (top panel), $a_{1+}^{\{2\},\hat{\boldsymbol{a}}}$ (middle panel), $a_{2+}^{\{2\},\hat{\boldsymbol{a}}}$ (bottom panel), as a function of Δj at collision energies of 15 meV (black open squares), 30 meV (red open circles) and 66 meV (blue open triangles) for the $f \rightarrow f$ spin–orbit conserving transitions.

FIG. 12. The CC QM $m_{j'}$ populations as a function of the scattering angle (black: no population, yellow: 0.5). Upper panels: Comparison of the $m_{j'}$ ($m_{j'}^{\hat{\boldsymbol{a}}}$) populations in the scattering frame for $E_{\rm coll} = 66$ meV, $\Delta j = 10$ (left) with that in the apse frame for the same transition and collision energy (right). Lower panels: Comparison of the $m_{j'}^{\hat{\boldsymbol{a}}}$ populations in the apse frame for $E_{\rm coll} = 15$ meV, $\Delta j = 5$ (left) with the apse frame populations for $E_{\rm coll} = 66$ meV, $\Delta j = 5$ (right). All data is for the $f \rightarrow f$, spin–orbit conserving transitions.

FIG. 13. The CC QM (black solid lines), apse model (red dashed lines), and heteronuclear hard shell (blue dashed-dotted lines) renormalized PDDCSs, $\rho_0^{\{2\}}(\theta)$ (top row), $\rho_{1+}^{\{2\}}(\theta)$ (middle row), and $\rho_{2+}^{\{2\}}(\theta)$ (bottom row), for the $\Delta j = 3$ (left column), $\Delta j = 10$ (middle column) and $\Delta j = 14$ (right column) transitions. The open-shell CC QM data have been averaged over initial and summed over final Λ-doublet state.

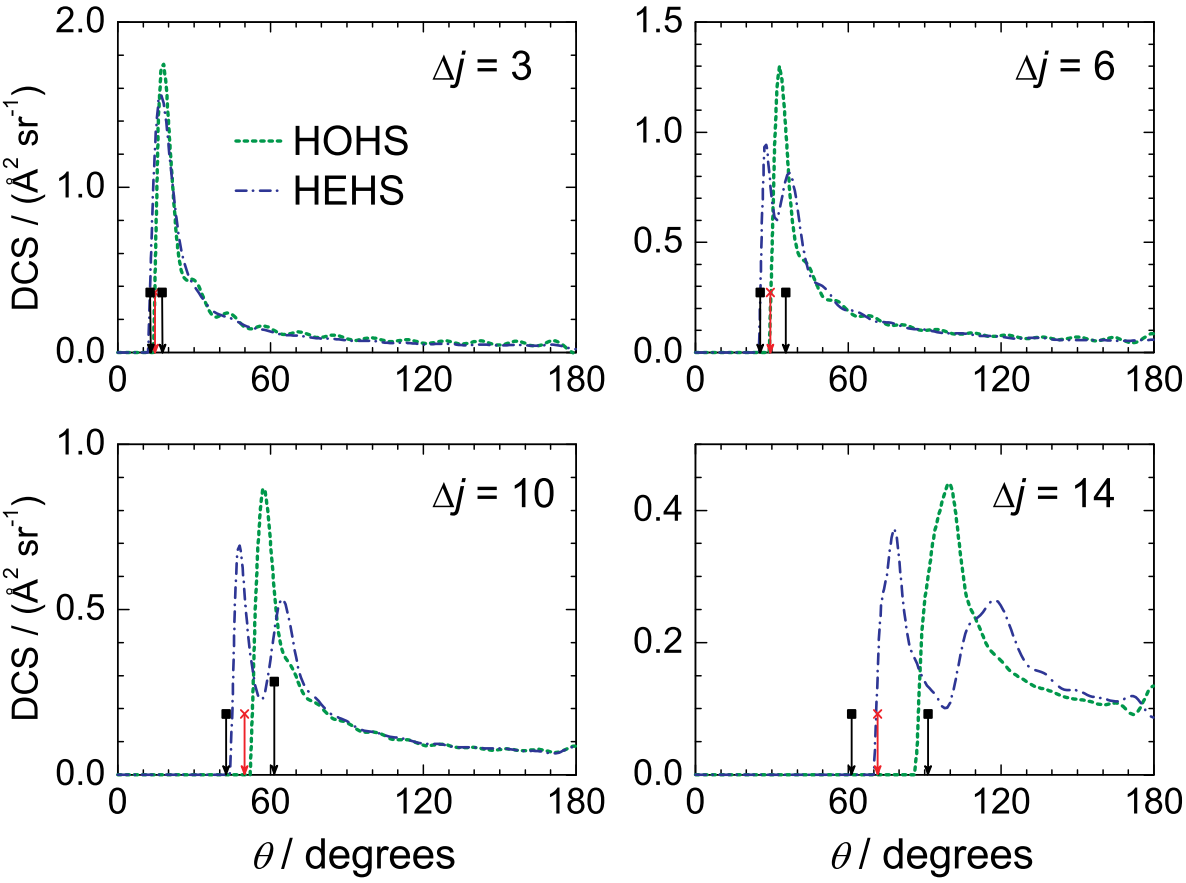
Δj = 3
HOHS
HEHS
Δj = 6
Δj = 10
Δj = 14
DCS / (Å² sr⁻¹)
θ / degrees
0.0
0.5
1.0
1.5
2.0
0.2
0.4
0
60
120
180

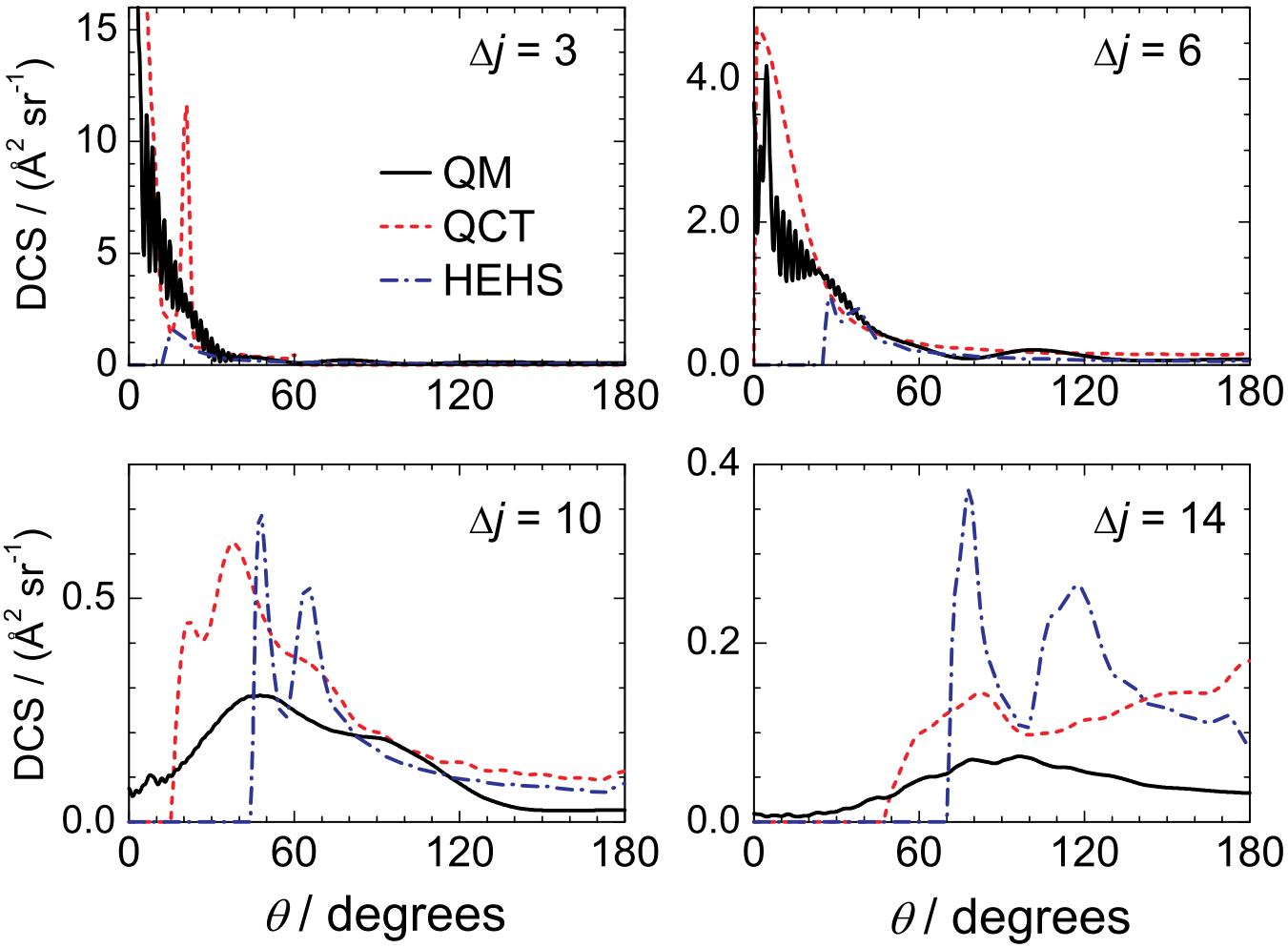
Δj = 3
Δj = 6
Δj = 10
Δj = 14
QM
QCT
HEHS
DCS / (Å² sr⁻¹)
θ / degrees
0
60
120
180
15
10
5
4.0
2.0
0.5
0.4
0.2

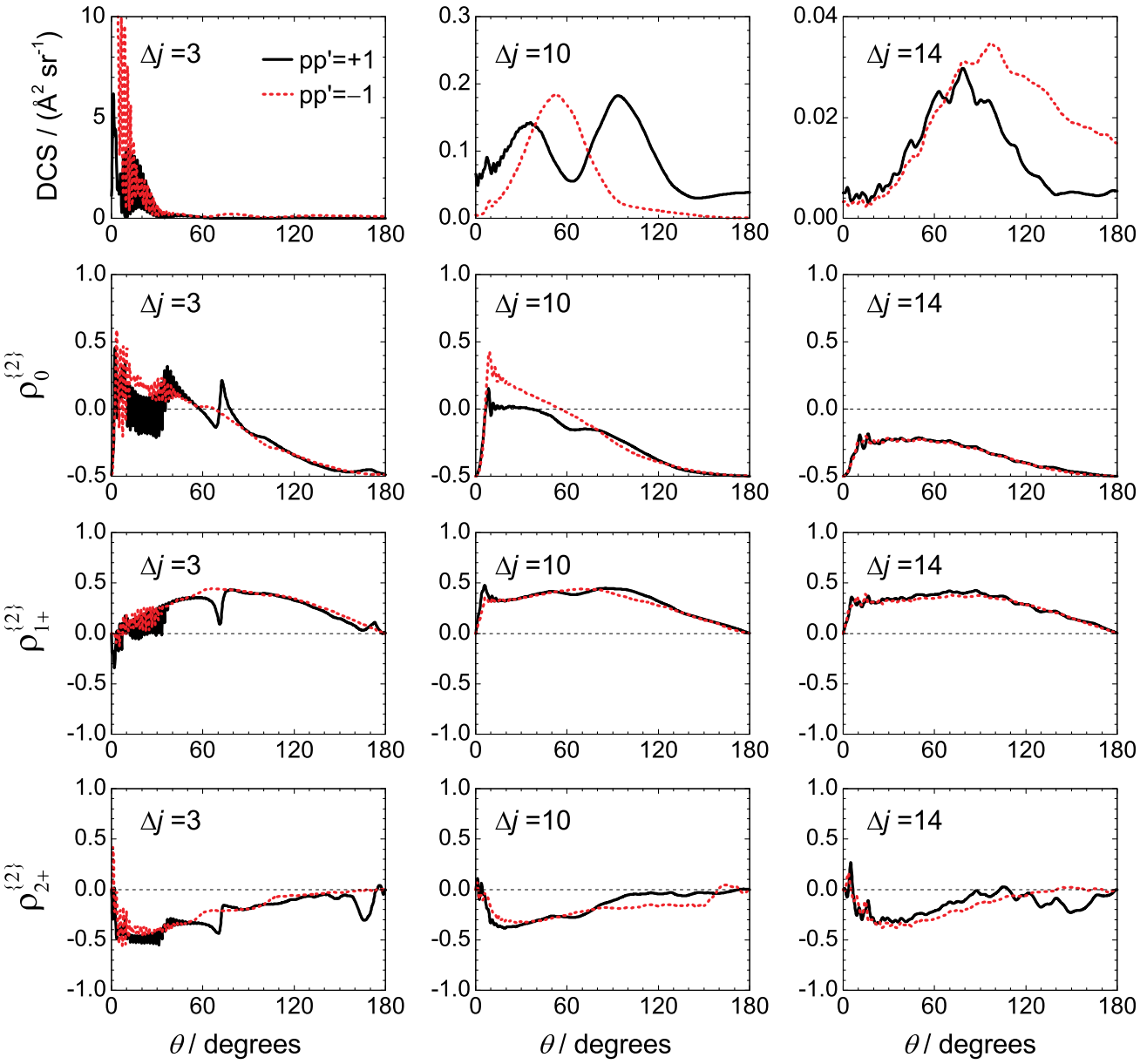
DCS / (Å^2 sr^{-1})
Δj =3
pp'=+1
pp'=−1
Δj =10
Δj =14
$\rho_0^{\{2\}}$
$\rho_{1+}^{\{2\}}$
$\rho_{2+}^{\{2\}}$
θ / degrees

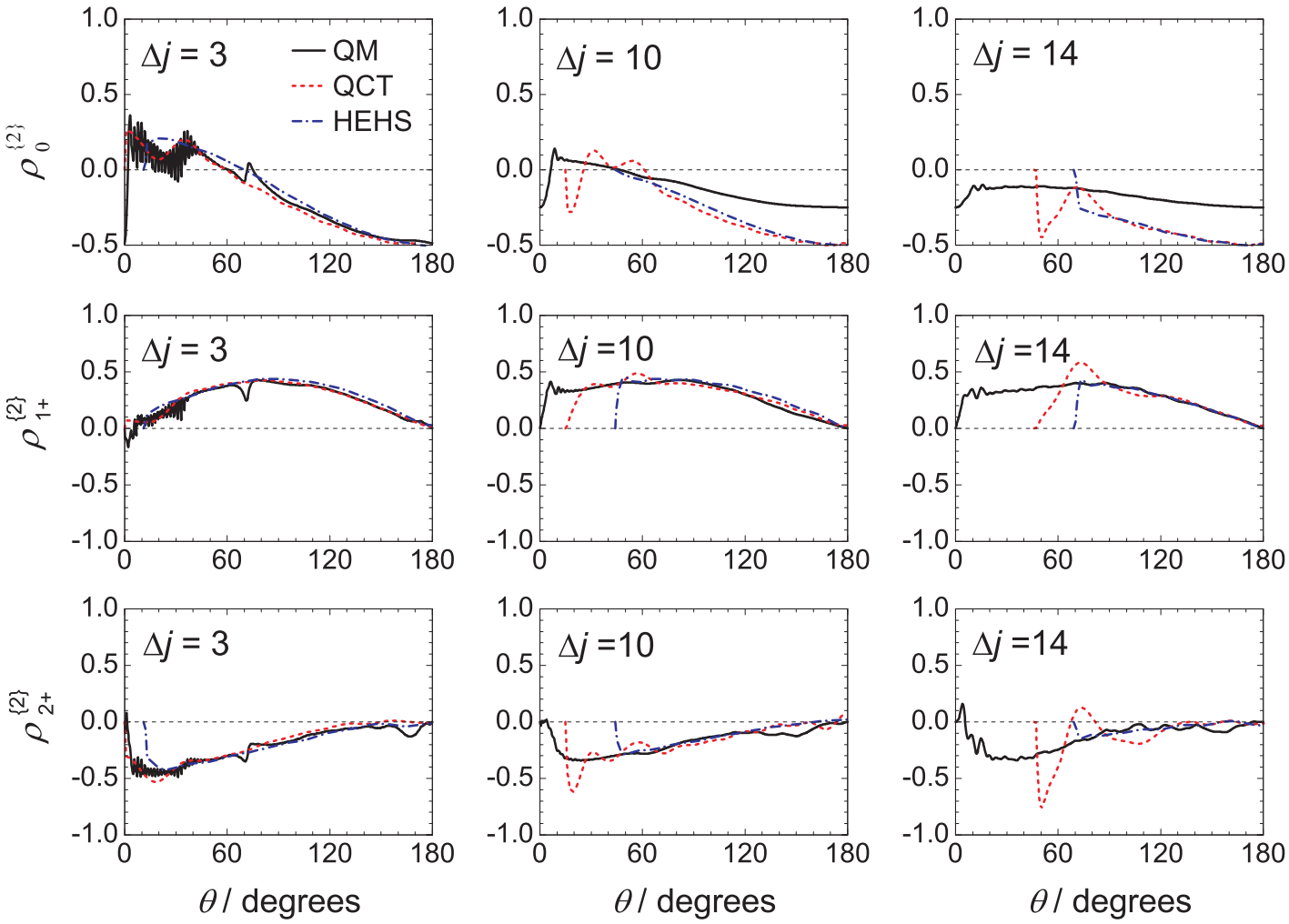
Δj = 3
QM
QCT
HEHS
Δj = 10
Δj = 14
Δj =10
Δj =14
ρ {2} 0
ρ {2} 1+
ρ {2} 2+
θ / degrees
1.0
0.5
0.0
-0.5
-1.0
0
60
120
180

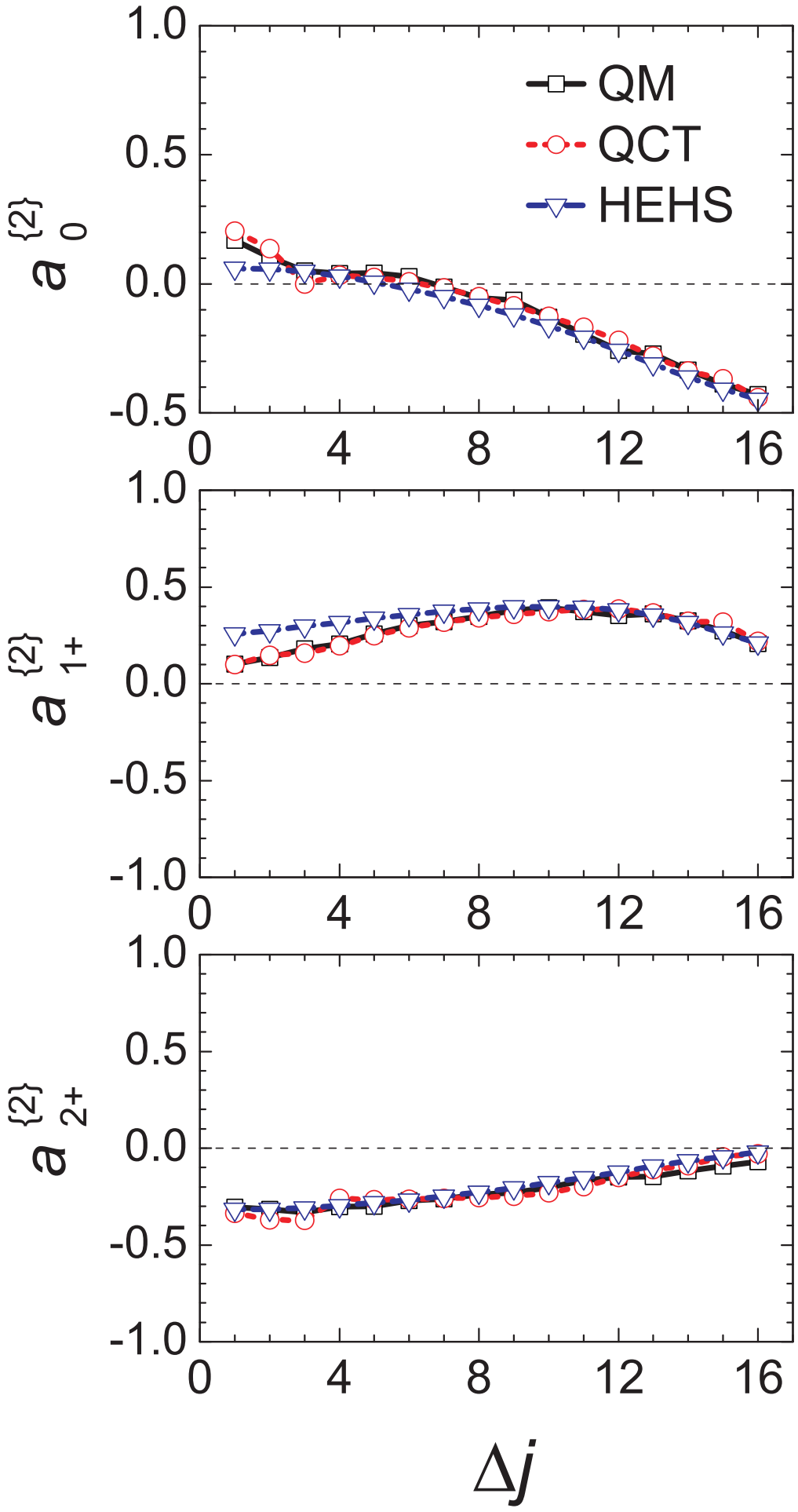
QM
QCT
HEHS
$a^{\{2\}}_{0}$
$a^{\{2\}}_{1+}$
$a^{\{2\}}_{2+}$
1.0
0.5
0.0
-0.5
-1.0
0
4
8
12
16
Δj

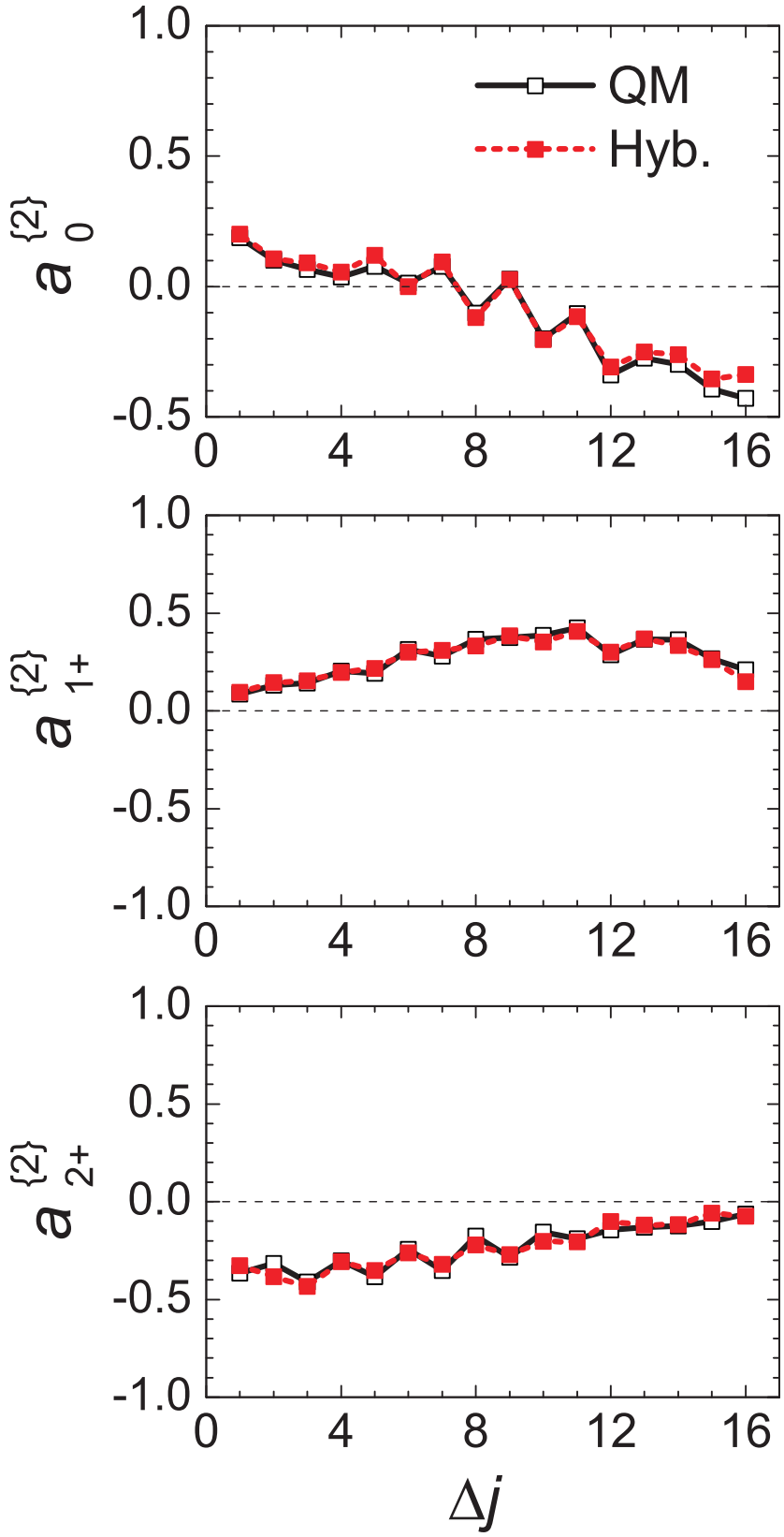
QM
Hyb.
$a^{\{2\}}_{0}$
$a^{\{2\}}_{1+}$
$a^{\{2\}}_{2+}$
1.0
0.5
0.0
-0.5
-1.0
0
4
8
12
16
Δj

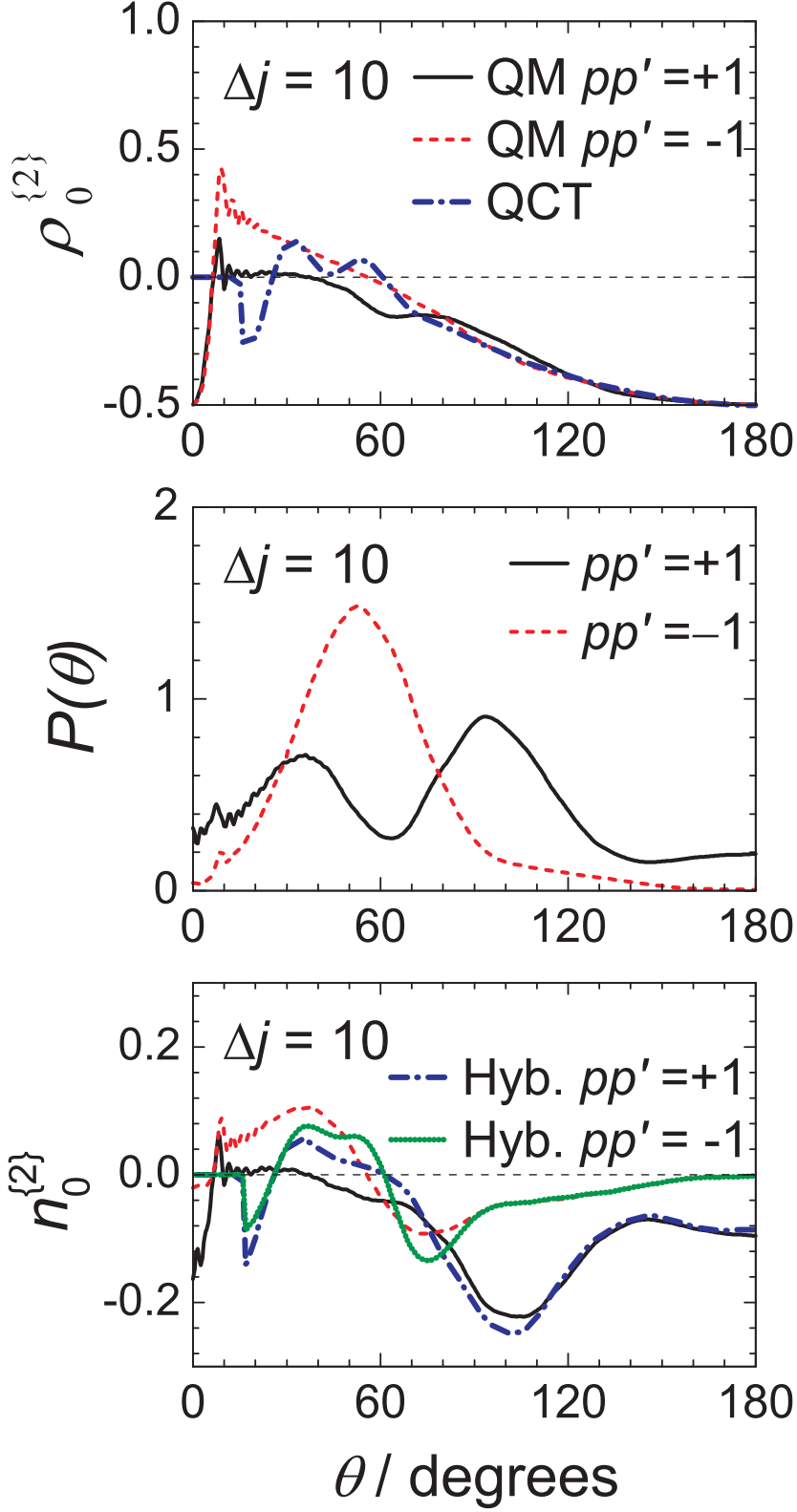
Δj = 10
QM pp′ =+1
QM pp′ = -1
QCT
$\rho_0^{\{2\}}$
1.0
0.5
0.0
-0.5
0
60
120
180
Δj = 10
pp′ =+1
pp′ =–1
P(θ)
2
1
0
0
60
120
180
Δj = 10
Hyb. pp′ =+1
Hyb. pp′ = -1
$n_0^{\{2\}}$
0.2
0.0
-0.2
0
60
120
180
θ / degrees

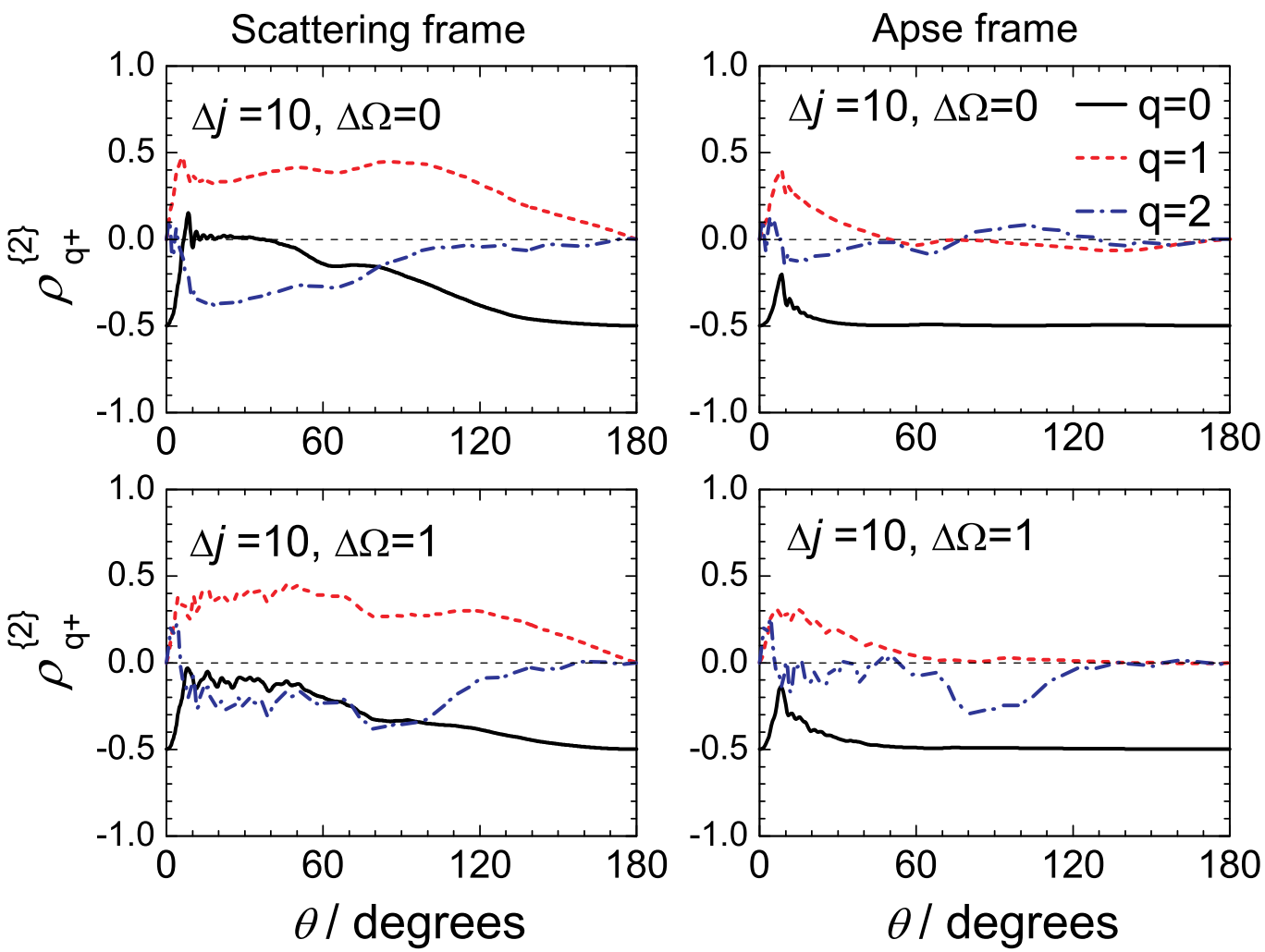
Scattering frame
Apse frame
Δj =10, ΔΩ=0
Δj =10, ΔΩ=1
q=0
q=1
q=2
ρ {2} q+
θ / degrees
1.0
0.5
0.0
-0.5
-1.0
0
60
120
180

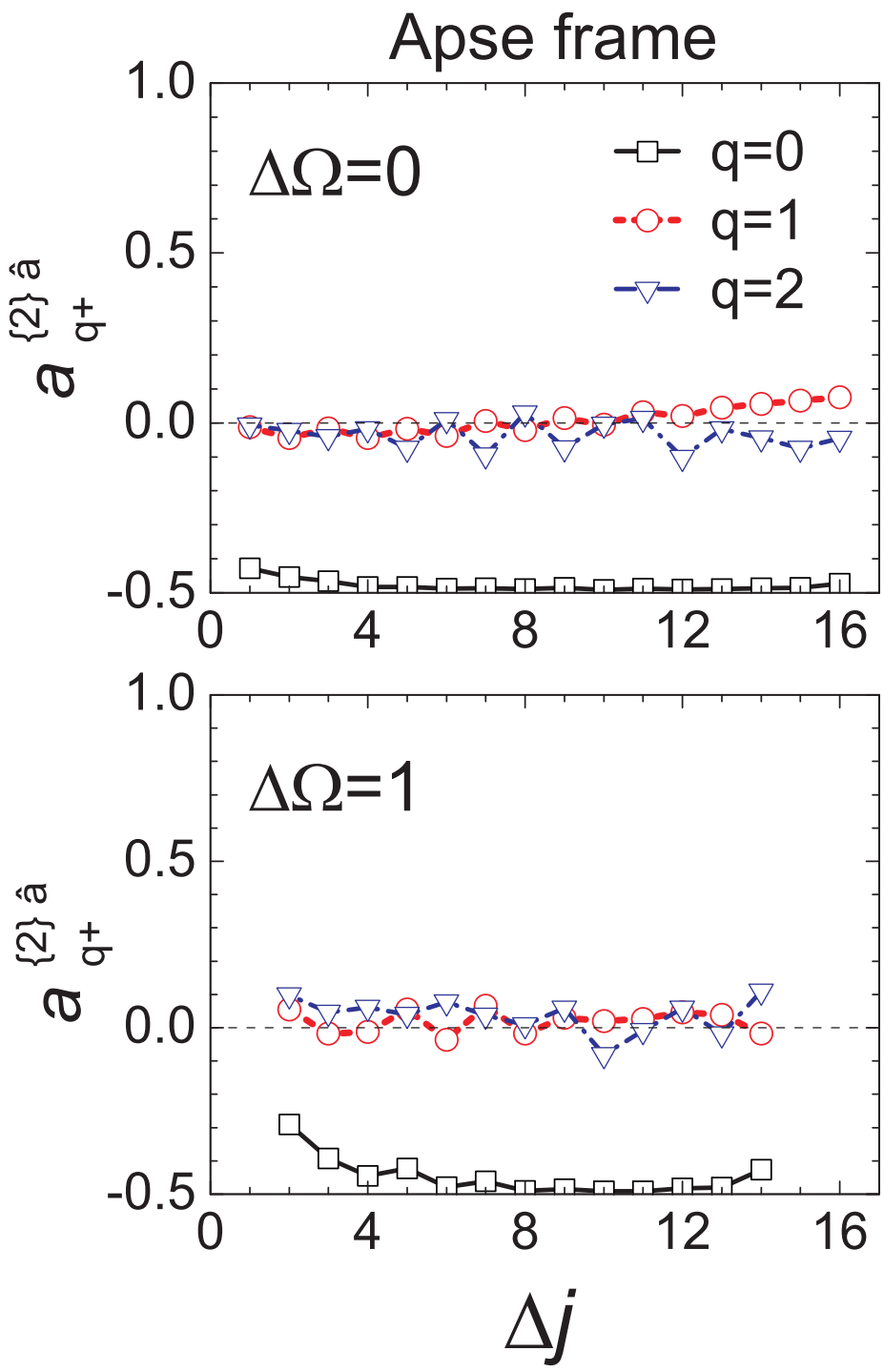
Apse frame
ΔΩ=0
q=0
q=1
q=2
ΔΩ=1
1.0
0.5
0.0
-0.5
0
4
8
12
16
Δj

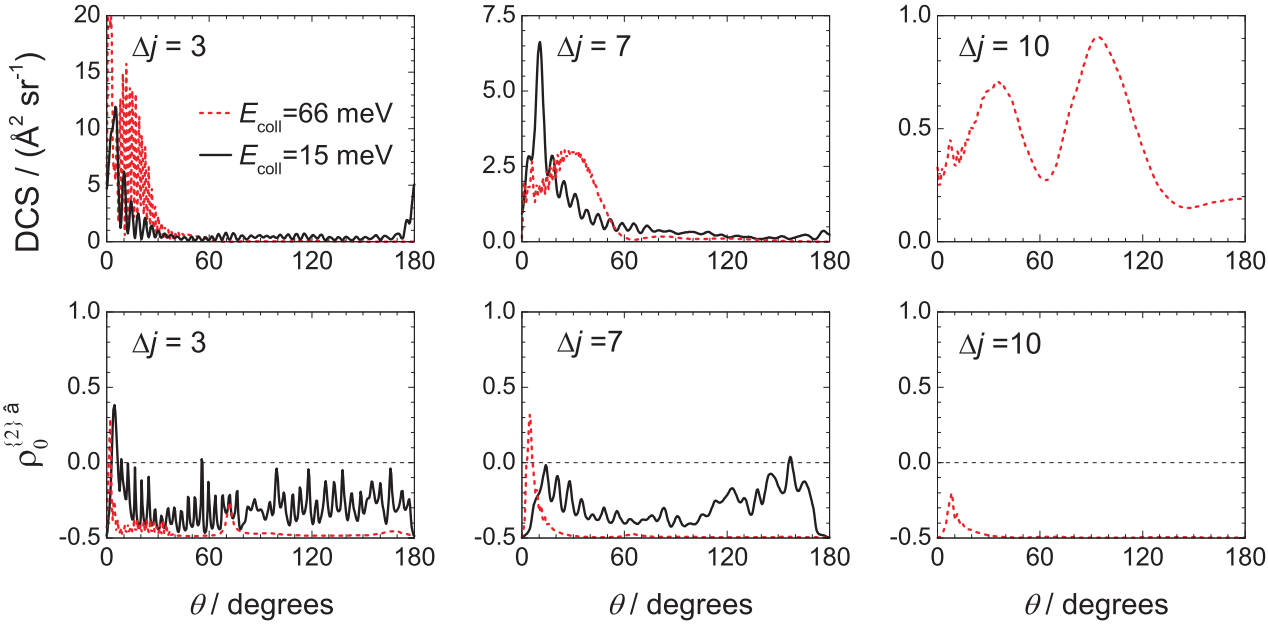
DCS / (Å^2 sr^{-1})
Δj = 3
E_{coll}=66 meV
E_{coll}=15 meV
Δj = 7
Δj = 10
$\rho_0^{\{2\}}$(â)
Δj = 3
Δj =7
Δj =10
θ / degrees
θ / degrees
θ / degrees

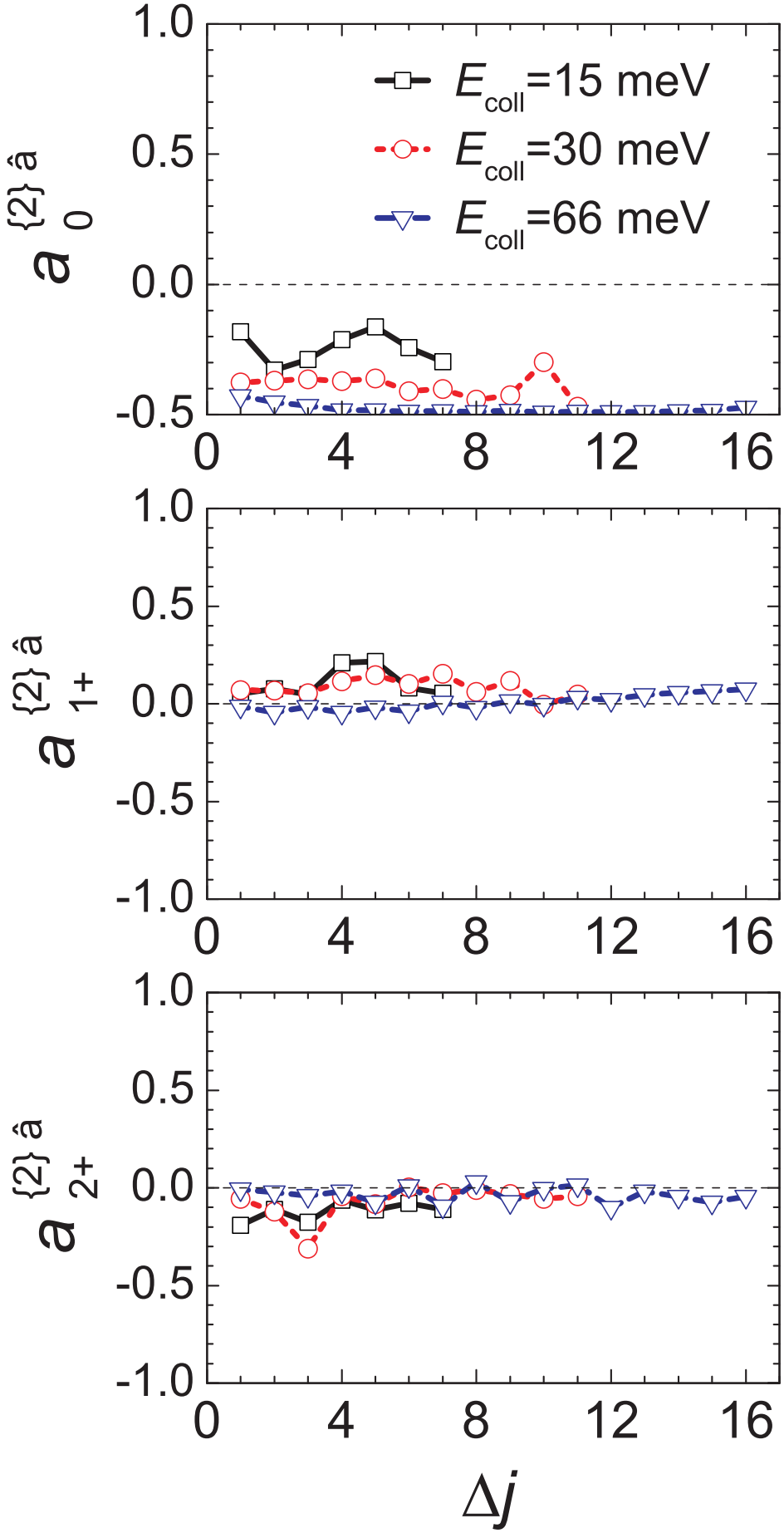
E_{coll}=15 meV
E_{coll}=30 meV
E_{coll}=66 meV
$a^{\{2\}}_{0}$
$a^{\{2\}}_{1+}$
$a^{\{2\}}_{2+}$
1.0
0.5
0.0
-0.5
-1.0
0
4
8
12
16
Δj

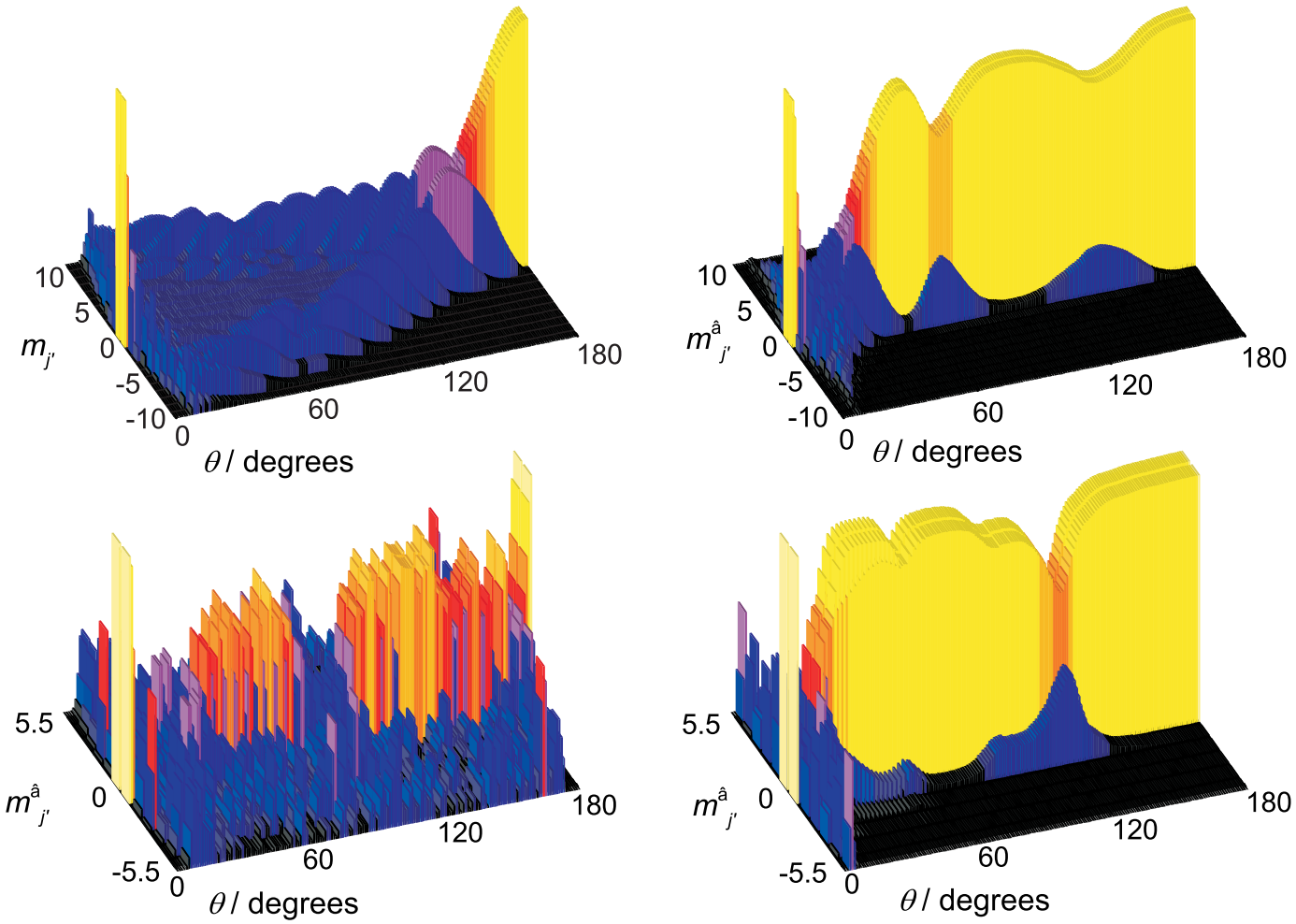
10
5
0
-5
-10
$m_{j'}$
0
60
120
180
θ / degrees
10
5
0
-5
-10
$m^{\hat{a}}_{j'}$
0
60
120
180
θ / degrees
5.5
0
-5.5
$m^{\hat{a}}_{j'}$
0
60
120
180
θ / degrees
5.5
0
-5.5
$m^{\hat{a}}_{j'}$
0
60
120
180
θ / degrees

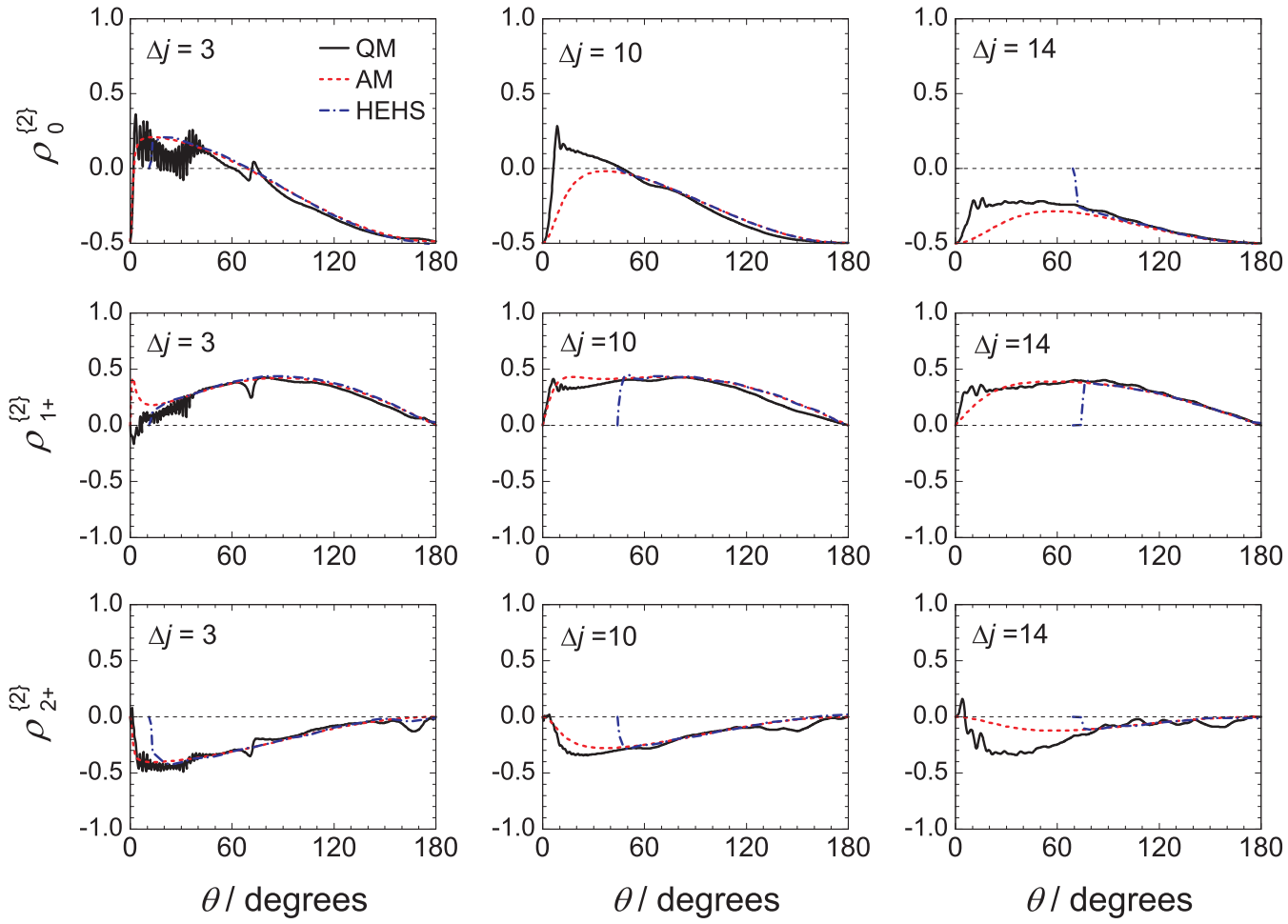
Δj = 3
QM
AM
HEHS
Δj = 10
Δj = 14
Δj =10
Δj =14
ρ {2} 0
ρ {2} 1+
ρ {2} 2+
θ / degrees
1.0
0.5
0.0
-0.5
-1.0
0
60
120
180